RESEARCH ARTICLE

Key Points:
- Hourly surface fluxes are produced with an inverse method over the north-western Mediterranean, during 1 year at a fine scale
- With the fluxes deduced from the inverse method, the annual heat and water budgets are closed within some $W\,m^{-2}$ and some $mm\,yr^{-1}$
- Compared with the adjusted fluxes, numerical prediction models are evaluated: they fail to retrieve the mean patterns and values

Correspondence to:
G. Caniaux,
guy.caniaux@meteo.fr

An inverse method to derive surface fluxes from the closure of oceanic heat and water budgets: Application to the north-western Mediterranean Sea

G. Caniaux[1] (ID), L. Prieur[2] (ID), H. Giordani[1] (ID), and J.-L. Redelsperger[3]

[1]CNRM-UMR3589 (Météo-France/CNRS), Toulouse, France, [2]Sorbonne Universités, UPMC Univ. Paris 06, INSU-CNRS-UMR7093, Laboratoire d'Océanographie de Villefranche, Villefranche-sur-Mer, France, [3]UBO/CNRS-UMR6523, Brest, France

Abstract The large amount of data collected during DeWEX, MOOSE, and HyMeX campaigns in the north-western Mediterranean in 2012–2013 allowed to implement an inverse method to solve the difficult problem of heat and water budget closure. The inverse method is based on the simulation of the observed heat and water budgets, strongly constrained by observations collected during the campaigns and on the deduction of adjusted surface fluxes. The inverse method uses a genetic algorithm that generates 50,000 simulations of a single-column model and optimizes some adjustable coefficients introduced in the surface fluxes. Finally, the single-column model forced by the adjusted fluxes during 1 year and over a test area of about $300 \times 300\ km^2$ simulates the daily mean satellite bulk SST with an accuracy/uncertainty of $0.011 \pm 0.072°C$, as well as daily mean SSS and residual buoyancy series deduced from wintertime analyses with an accuracy of 0.011 ± 0.008 and $0.03 \pm 0.012\ m^2\,s^{-2}$, respectively. The adjusted fluxes close the annual heat and rescaled water budgets by less than $5\ W\,m^{-2}$. To our knowledge, this is the first time that such a flux data set is produced. It can thus be considered as a reference for the north-western Mediterranean and be used for estimating other flux data sets, for forcing regional models and for process studies. Compared with the adjusted fluxes, some operational numerical weather prediction models (ARPEGE, NCEP, ERA-INTERIM, ECMWF, and AROME), often used to force oceanic models, were evaluated: they are unable to retrieve the mean annual patterns and values.

1. Introduction

The knowledge of surface fluxes exchanged between the ocean and the atmosphere has important issues: forcing oceanic models, studying the processes by which the ocean and the atmosphere exchange energy, mass, and momentum, getting climatological estimates of the variability of ocean surface forcings, and evaluating their role in the Earth's climate system. In the last 20 years, lots of gridded air-sea flux fields, derived from in situ observation analyses, from numerical model reanalyses, from satellite retrievals or from merging satellite, and numerical model outputs were produced [e.g., *Large and Yeager*, 2009; *Valdivieso et al.*, 2015; G. Jordà et al., The Mediterranean Sea heat and mass budgets: Estimates, uncertainties and perspectives, submitted to *Progress in Oceanography*, 2017]. However, surface flux fields are difficult to estimate because they are highly dependent (1) of the biases which affect empirical bulk formulae, (2) of uncertainties in exchange coefficients (especially at low and high winds), (3) of imperfect boundary layer parameterizations [*Cronin et al.*, 2014], and (4) of the spatial and temporal resolutions of flux-related variables [*Artale et al.*, 2002; *Ruti et al.*, 2008]. In consequence, few flux data sets are able to close budgets for the global ocean [*Valdivieso et al.*, 2015] or at basin scale [*Castellari et al.*, 1998; *Sanchez-Gomez et al.*, 2011]. Urgent improvements are also needed for radiative [*Liu et al.*, 2015] and water budgets [*Bowman et al.*, 2009; *Romanou et al.*, 2010] (for the Mediterranean).

Moreover, errors and uncertainties affecting fluxes lead forced oceanic models or coupled models to diverge [*Rosati and Miyakoda*, 1988]. Generally modelers use restoring terms in the scalar equations to prevent the model solution to drift from prescribed values or from the mean climatological state [*Barnier et al.*, 1995]. However, relaxation techniques alter and modify the model thermodynamics and may produce

distortions in annual cycles [*Killworth et al.*, 2000], and over longer time scales, may alter or even suppress some internal modes of variability [*Simmons and Polyakov*, 2004]. Another expedient consists in correcting surface fluxes [*Large and Yeager*, 2009; *Pettenuzzo et al.*, 2010]. For that, many techniques have been used in different regions of the world ocean in order to close heat and water budgets or at least to be consistent with some constraints (see the review by *Large and Yeager* [2009]). Some include inverse methods by imposing oceanic constraints, like observed transports [*Isemer et al.*, 1989; *MacDonald and Wunsch*, 1996], and mixed layer heat contents [*Gaspar et al.*, 1990b] or atmospheric constraints, i.e., mass, moisture, and energy budgets [*Trenberth*, 1997], temperature Q1 and humidity Q2 budgets [*Curry et al.*, 1999]. Other studies propose linear inverse analyses by using heat flux constraints [*Grist and Josey*, 2003], or assimilation of observations in numerical models with the adjoint equation formalism of a one-dimensional [*Roquet et al.*, 1993] or three-dimensional modeling approach [*Stammer et al.*, 2004; *Yuan and Rienecker*, 2003; *Groeskamp et al.*, 2014]. Variational objective analyses are another alternative to obtain best estimates of meteorological variables needed to estimates surface fluxes [e.g., *Yu et al.*, 2004; *Yu and Weller*, 2007].

Caniaux et al. [2005b] tested an inverse method based on the optimization of numerous model runs by a genetic algorithm to produce adjusted fluxes at a rather fine scale, in order to study subduction in the north-eastern Atlantic. They showed that, if the region of study was well sampled during a relatively long period of time (the POMME experiment in 2000–2001) [*Mémery et al.*, 2005], the inverse method was particularly suitable to produce surface fluxes and to simulate realistically the oceanic upper layers without any correction or restoring term [*Paci et al.*, 2005; *Giordani et al.*, 2005] and to deduce reliable seasonal and annual subduction rates [*Paci et al.*, 2007]. Here we address the same question in a different context and region, i.e., in the north-western Mediterranean (NWM).

The NWM is much more energetic than the intergyre region of the north-eastern Atlantic. The basin is characterized by the presence of the Northern Mediterranean Current (or Liguro-Provençal Current), which flows south westward along the continental margin [*Millot*, 1987], and further south by the north-eastward return flow marked by the eddying Balearic front around 40°N [*Send et al.*, 1999; *Poulain et al.*, 2012]. The NWM is also known to form dense waters, the Western Mediterranean Deep Waters (WMDW), during deep convective events [*Rhein*, 1995; *Marshall and Schott*, 1999]. Another difference is that surface fluxes are dominated by frequent continental gale force winds [*Bourassa et al.*, 2013], associated with cold and dry air masses that contrast significantly with the SSTs to generate important heat loss [*Leaman and Schott*, 1991], i.e., in conditions where the errors and uncertainties which affect the bulk formulae are the largest. Moreover, fine temporal and spatial resolution fluxes are crucial for simulating correctly both the intensity and timing of intense mixing and deep oceanic convection, given the low Rossby radius reached in winter and the stochastic nature of the mechanisms at play [*Castellari et al.*, 2000; *Herrmann and Somot*, 2008; *Béranger et al.*, 2010]. There is also a clear need of accurate surface fluxes at fine temporal and spatial scales to produce realistic estimates of dense water formation rates in the NWM [*Durrieu de Madron et al.*, 2013; *Waldman et al.*, 2016].

As the NWM was extensively sampled from summer 2012 to summer 2013, with still more numerous in situ data than during the POMME campaigns, mostly due to gliders (nonexistent in 2000–2001) and to an increased number of ARGO floats, an attempt to test *Caniaux et al.*'s [2005b] inverse method is exposed in the present paper. During one annual cycle, the NWM was investigated in the frame of three scientific programs: the Mediterranean Ocean Observing System for the Environment (MOOSE) [*Testor et al.*, 2012, 2013], the Mediterranean Pelagic Ecosystems Experiment (DeWEX) [*Testor*, 2013; *Conan*, 2013], and the Hydrological Cycle of the Mediterranean Experiment (HyMeX) [*Drobinski et al.*, 2014].

The paper is organized as follows: section 2 provides a description of the single-column model (SCM) and the inverse method approach. Data used and the forcings of the SCM are presented in section 3, and results including the optimized corrections in section 4. In section 5, a local evaluation of the adjusted fluxes against in situ data, an evaluation of some numerical weather prediction models (NWPM) fields and an estimate of the heat and water budget closure are provided. Conclusions are drawn in section 6. Note that the SCM presented in section 2 can be used not only to optimize surface forcings but also to study the physics of the near-surface layers; for instance, to investigate the different processes at play in the evolution of SSTs, SSSs, of temperature and salinity profiles, stratification, and so on. A brief outline of this use of the SCM can be found in section 4.2.

2. The Inverse Method

The objective of this work is to find the best heat, water, and momentum fluxes that allow to simulate the evolution of a water column as close as possible to the observed one. For this purpose, an inverse method has been developed in applying a suitable optimization method which uses a stochastic algorithm (here a genetic algorithm based on natural selection). Such stochastic algorithms are widely applied for optimization problems in physical [e.g., *Sumata et al.*, 2013, and references therein] or biogeochemical modeling [e.g., *Shigemitsu et al.*, 2012].

For applying this method, a SCM is first implemented to simulate the evolution of the water column. The SCM is able to predict the heat, salt and momentum evolutions and is adapted to simulate a given area of the NWM (section 2.1). From an initial estimate of the surface fluxes (hereafter called the "a priori fluxes"), the model, constrained through the balance between lateral advection and surface fluxes, is able to simulate during 1 year the evolution of the mean temperature and salinity profiles in this area.

We then introduce a cost function to compute the model – data misfit of satellite SSTs, analyzed SSSs, observed temperature and salinity profiles as well as analyzed residual buoyancies. By varying some adjustment coefficients (the control parameters) introduced for correcting the fluxes, an optimal set of these coefficients is derived from the minimization of the cost function with the genetic algorithm (presented in section 2.2). The method has been implemented on a simulation test area defined in section 3.1 with a careful determination of all the forcings needed to carry out the SCM simulations (see section 3.2). The optimization of the cost function allows to correct the a priori fluxes at any time step and any grid point of the test area, and of a somewhat larger surface area.

2.1. The Single-Column Model (SCM)

The SCM used is derived from the one-dimensional numerical model of vertical mixing developed by *Gaspar et al.* [1990a] and updated by *Wade et al.* [2011]. This model solves the heat, salt, and momentum equations of a water column and is closed by a 1.5 turbulent scheme solving a turbulent kinetic energy (TKE) equation.

The turbulent vertical fluxes are parameterized using the concept of eddy diffusivity in which the fluxes are expressed as $\overline{X'w'} = -K_X \partial_z X$, where X represents any variable of the model (momentum u and v, and scalar variables T and S). The calculation of K_X is related to the local TKE (noted $\bar{e}$) with a mixing length scale l_k determined from physical considerations and a calibration constant c_k by the following equation: $K_X = c_k l_k \sqrt{\bar{e}}$. The mixing length l_k is derived from the balance between TKE and potential energy. The reader can refer to *Gaspar et al.* [1990a] for further details of the parameterization. The model also includes a parameterization of diapycnal mixing [*Large et al.*, 1994; *Kantha and Clayson*, 1994] to better represent nonlocal sources of vertical mixing under the mixed layer depth. The model includes 450 regularly spaced levels of five meters with the first level of temperature, salinity and current located at a depth of 2.5 m below the surface. The first level temperature will thus be assimilated with a bulk SST and considered as such in all this study, implying that it can be easily compared with satellite SSTs used in the following sections. Vertical turbulent mixing is solved with a semiimplicit numerical scheme. The time step is 1 h.

For the present study, the model was switched into a SCM to take into account advection terms considered as external forcings and added at each time step in the equations so that the SCM can simulate a large water column representing part of the NWM (referred hereafter as the test area). The problem is to solve the equations of the temperature and salinity averaged over the test area itself, as well as their subgrid-scale fluctuations. For that, we consider the three-dimensional temperature T equation:

$$\partial_t T = \underbrace{\frac{F_{sol}}{\rho_0 C_p} \partial_z I}_{\text{solar radiation}} - \underbrace{\vec{u}.\vec{\nabla}_h T}_{\text{horizontal advection}} - \underbrace{w \partial_z T}_{\text{vertical advection}} - \underbrace{\nabla_h.\left(\overline{T'.\vec{u'}}\right)}_{\text{horizontal diffusion}} - \underbrace{\partial_z\left(\overline{T'w'}\right)}_{\text{vertical diffusion}} \tag{1}$$

$$\underbrace{}_{\text{tendency}}$$

where the temperature tendency results from net solar radiation input F_{sol}, horizontal and vertical advections, horizontal and vertical diffusions. The single primes refer to the unresolved turbulent scales involved; $\partial_z I$ is the fraction of F_{sol} that penetrates at depth z; ρ_0 and C_p are a reference surface density and the specific heat capacity of sea water, respectively.

The horizontal and vertical advection terms were partitioned into Ekman (the horizontal Ekman current is denoted $\vec{u_e}$ and the vertical Ekman velocity w_e) and non-Ekman components ($\vec{u_{ne}}$ and w_{ne}, respectively) so that (1) is rewritten as:

$$\underbrace{\partial_t T}_{tendency} = \underbrace{\frac{F_{sol}}{\rho_0 C_p}\partial_z I}_{solar\ radiation} \underbrace{- \vec{u_e}.\vec{\nabla_h} T}_{Ekman} \underbrace{- \vec{u_{ne}}.\vec{\nabla_h} T}_{non-Ekman} \underbrace{- w_e\partial_z T}_{Ekman} \underbrace{- w_{ne}\partial_z T}_{non-Ekman} \underbrace{- \nabla_h.\overline{\left(T'.\vec{u'}\right)}}_{horizontal\ diffusion} + \underbrace{\partial_z(K\partial_z T)}_{vertical\ diffusion} \tag{2}$$

$$\underbrace{\qquad\qquad}_{horizontal\ advection} \qquad \underbrace{\qquad\qquad}_{vertical\ advection}$$

in which the vertical turbulent fluxes ($-\overline{T'w'}$) in the vertical diffusion term of equation (1) were parameterized using the concept of eddy diffusivity ($K\partial_z T$).

In *Caniaux et al.* [2005b], the horizontal and vertical non-Ekman advection terms were altogether derived from the evolution of mean temperature and salinity profiles deduced from four hydrological surveys performed during the 1 year of the POMME experiment (see reference in the introduction). This hypothesis was valid as long as advection was a weak term in comparison with the other processes, not only near the surface but also at depth. This technique could not be used any more, since horizontal advection in the NWM is highly depth dependent and plays a much more important role in the top layers than at deeper levels (see sections 3.2.3 and 4.2). This led us to hypothesize that the horizontal non-Ekman advection term could be represented by geostrophic advection, a term that could easily be deduced from the outputs of a three-dimensional 3-D model run (see section 3.2.3).

As some nonlinear terms in equation (2) cannot be explicitly calculated at any point of the test area, they were split into spatial mean and deviation from the mean. This is the case for solar radiation, vertical Ekman advection and vertical diffusion (respectively, the first, fourth, and last terms of equation (2)). After decomposing these terms into their spatial mean (denoted by angle brackets) and deviation (denoted by double prime), and after averaging each term over the test area (again with angle brackets) so that the SCM can simulate one single column representative of the whole test area, equation (2) becomes:

$$\underbrace{\langle\partial_t T\rangle}_{tendency} = \underbrace{\frac{\langle F_{sol}\rangle}{\rho_0 C_p}\partial_z\langle I\rangle}_{mean} + \underbrace{\frac{\langle F_{sol}''\partial_z I''\rangle}{\rho_0 C_p}}_{deviation} - \underbrace{\langle\vec{u_e}.\vec{\nabla_h} T\rangle}_{Ekman} - \underbrace{\langle\vec{u_{ne}}.\vec{\nabla_h} T\rangle}_{non-Ekman} - \underbrace{\langle w_e\rangle\partial_z\langle T\rangle}_{mean} - \underbrace{\langle w_e''\partial_z T''\rangle}_{deviation} - \underbrace{\langle w_{ne}\partial_z T\rangle}_{non-Ekman}$$

$$\underbrace{\qquad\qquad}_{solar\ radiation} \qquad \underbrace{\qquad\qquad}_{horizontal\ advection} \qquad \underbrace{\qquad\qquad\qquad}_{Ekman}$$
$$\underbrace{\qquad\qquad\qquad\qquad}_{vertical\ advection}$$

$$- \underbrace{\langle\nabla_h.\overline{\left(T'.\vec{u'}\right)}\rangle}_{horizontal\ diffusion} + \underbrace{\partial_z(\langle K\rangle\partial_z\langle T\rangle)}_{mean} + \underbrace{\partial_z\langle K''\partial_z T''\rangle}_{deviation} \tag{3}$$
$$\underbrace{\qquad\qquad\qquad}_{vertical\ diffusion}$$

The area mean component of the solar radiation, the horizontal Ekman advection and the horizontal non-Ekman advection terms were evaluated explicitly from the data available at each grid point of the test area (see sections 3.2.1–3.2.3 where we explain how these terms were computed) before being averaged over this area. Similarly, the mean vertical Ekman advection term was estimated by calculating a vertical Ekman velocity w_e from the wind stress curl at each grid point of the test area before averaging and from the area mean vertical profile of temperature <T> calculated by the SCM (see section 3.2.4). The mean vertical diffusion term was computed by the SCM through its vertical mixing parameterization and from the upper boundary conditions, i.e., from the surface turbulent fluxes estimated at each grid point of the test area before averaging:

$$-\langle\overline{T'w'}(0)\rangle = \frac{\langle H\rangle + \langle L\rangle + \langle F_{LW}\rangle}{\rho_0 C_p}$$

$$-\langle\overline{S'w'}(0)\rangle = \langle E\rangle - \langle P\rangle \tag{4}$$

$$-\langle\overline{w'.\vec{u'}}(0)\rangle = \frac{\langle\vec{\tau}\rangle}{\rho_0}$$

respectively, for the temperature, salinity and current equations. In equation (4), H, L, and F_{LW} represent the sensible (H), latent (L), and net longwave radiation (F_{LW}); E and P are the evaporation and precipitation rates

(expressed in m s^{-1}), respectively, and $\vec{\tau}$ is the surface wind stress. In this study, the surface heat fluxes are counted positive downward. For the vertical diffusion, the deviation term was parameterized since no data could provide an evaluation of this term across the test area (see section 3.2.5).

2.2. The Cost Function and the Genetic Algorithm

In the present study, the cost function (CF) expresses the misfit model-data and is defined as follows:

$$CF = \sum_i [obs - G(m)]^T W_i [obs - G(m)] \tag{5}$$

in which $obs = [x_1, x_2, \ldots, x_{Ni}]^T$ are observational data, $m = [m_1, m_2, \ldots, m_M]^T$ the set of M control parameters to be optimized by the genetic algorithm; $G(m) = [G_1(m), G_2(m), \ldots, G_{Ni}(m)]^T$ is the convolution of measurement function with the SCM, in which $G_n(m)$ is the modeled counterpart to the observational data. W_i are weighting matrix, which take into account uncertainties of the observational data. We consider the diagonal elements of the matrix W_i in the form $\frac{\alpha_i}{\sigma_i^2}$ where α_i represent the various contributions of the observational data and σ_i^2 their variance along the simulation. Here the observational data set is composed of the area mean satellite SSTs ($i = 1$ in equation (5)), analyzed SSSs ($i = 2$), observed temperature and salinity profiles ($i = 3$ and $i = 4$, respectively) available during the various surveys performed during the period 1 August 2012 to 31 July 2013, as well as the residual buoyancy ($i = 5$) deduced from analyses.

SSTs are the area mean daily satellite series during the period of simulation ($N_1 = 365$ days). SSSs and residual buoyancies (the residual buoyancy is defined as $RB = \int_{-H_0}^0 zN^2 dz$ in which $N^2(z)$ is the Brunt-Väisala frequency computed from *McDougall* [1987] and H_0 depth of the ocean, 2250 m) were obtained from daily objective analyses performed by one of the coauthors [*Giordani et al.*, 2014] for the winter period from mid-January to mid-May 2013 ($N_2 = N_5 = 119$ days) from all the data collected in the NWM (i.e., gliders, floats, CTDs, drifters, and satellite data). For the analyses, temperature and salinity data were first carefully checked to detect any erroneous values. They were then interpolated onto 800 vertical levels with a 5 m vertical resolution from the surface to the bottom and objectively analyzed onto a 1/12° horizontal grid following the procedure used by *Giordani et al.* [2005]. The first guess of the analyses was derived from the operational MERCATOR PSY2V4R4 model. At each grid point, the PSY2V4R4 analysis was corrected with the observations which lie within one influence time/space radius around the grid point, following the procedure of *De Mey and Ménard* [1989]. A space correlation radius of 10 km, consistent with the mesoscale structures of the NWM, and a decay *e*-folding time of 1 day were chosen. The diagonal elements of the matrix W_i were chosen inversely proportional to the number of data in the observational series and function of confidence we have in the quality of the data (i.e., 1, 0.8, 0.1, 0.1, and 0.1, respectively, for the SSTs, SSSs, CTD temperature and salinity profiles, and residual buoyancies).

The optimization of the M control parameters of the cost function was carried out using a genetic algorithm [*Carroll*, 1996]. This tool is derived from genetics and population evolution. It is used for seeking the extreme of particularly complex functions, sometimes with discontinuities, like in numerical models. The genetic algorithm searches in a M-dimensional space the M parameters that minimize a cost function CF evaluated for each run of the SCM. In the algorithm, the set of M parameters to be optimized are coded in a binary form called chromosome. The algorithm starts with a randomly chosen population of chromosomes, after which it evaluates the fitness value of each chromosome by computing a cost function, using the corresponding set of parameters to run the model. Then, the three genetic processes of selection, crossover and mutation are performed upon the chromosomes in sequence. During the selection, chromosomes are copied in proportion to their fitness values based on a probability of selection. Crossover acts on the selected chromosomes, using a crossover probability: this operator selects a crossover site within paired strings and exchanges between the two chromosomes the parts located to the right of the crossover site. Last, mutation is applied to the chromosomes in order to maintain diversity. After these processes, the new chromosomes are compared to those of the previous generation, and accepted or rejected based on an update probability. The procedure is repeated until convergence or stopped by fixing a maximum number of generations. The output of the algorithm is a set of M optimal parameters obtained after running a generally high number of model simulations.

As control parameters for the optimization, two control parameters were selected from the model adjustable constants and five others were introduced to correct the surface fluxes such that $M = 7$ as listed in Table 1. The first two are two adjustable constants in the parameterization of the incoming solar radiation

Table 1. List of Control Parameters, With Their Range of Values and the Optimum Obtained With the Genetic Algorithm[a]

Parameter (Unit)	Description	Range of Values	Optimum	Uncertainty
R	Partition parameter in the solar radiation	0.3–0.7	0.463	0.059
d_2 (m)	Extinction depth in the blue-green light	5–25	20.000	3.500
β_w	Surface wind correction	0.8–1.2	1.066	0.044
β_{ws}	Correction of the wind stress transfer coefficient	0.5–1.0	0.750	0.061
β_l	Correction of the latent heat flux transfer coefficient	0.7–1.1	0.900	0.097
β_h (W m^{-2})	Correction of the sensible heat flux transfer coefficient	−10–+10	4.526	3.519
β_p	Correction of precipitation	0.6–1.2	1.138	0.147

[a]The values of the uncertainty on the control parameters were obtained by assuming an expected error of 5% on the fitness function of Figure 7.

function $I(z)$ in equation (3). This parameterization relies on the double exponential transmission profile proposed by *Paulson and Simpson* [1977]:

$$I(z) = R \ \exp\left(-\frac{z}{d_1}\right) + (1-R) \ \exp\left(-\frac{z}{d_2}\right) \tag{6}$$

where z is the depth. R denotes a partition parameter between the red and blue-green parts of the solar radiation spectrum penetrating down to the extinction depths d_1 and d_2, respectively. Generally, red light has a rapid attenuation in the upper few meters compared to blue-green light. Sensitivity tests proved that SST is very sensitive to d_2 and R but not to d_1. We thus decided to retain d_2 and R as control parameters and to fix d_1 as the value of the standard type III waters in *Jerlov*'s [1976] classification (i.e., $d_1 = 1.4$ m).

For the other control parameters, five coefficients were introduced in the expressions of the area mean surface fluxes. These coefficients are supposed to represent corrections to be brought either to the input parameters or to the exchange coefficients of the bulk formulae:

1. Coefficient β_w corresponds to the errors affecting the surface wind. This parameter plays an important role because it affects directly wind stress, latent and sensible heat fluxes, and horizontal and vertical Ekman advections.
2. Coefficients β_{ws} and β_l represent the uncertainty affecting the exchange coefficients of wind stress and of latent heat flux (and evaporation), respectively. Both are multiplicative factors.
3. For sensible heat flux, a bias β_h was introduced instead of a multiplicative factor, because sensible heat may frequently change sign in the NWM, air temperatures being frequently close to SSTs.
4. β_p for correcting satellite rainfall.

Finally, the fluxes forcing the SCM were written as:

$$\langle\tau\rangle = \beta_w^2 \beta_{ws} \langle\tau\rangle^*$$
$$\langle L\rangle = \beta_l \beta_w \langle L\rangle^*$$
$$\langle H\rangle = \beta_w \langle H\rangle^* + \beta_h \tag{7}$$
$$\langle P\rangle = \beta_P \langle P\rangle^*$$

in which τ stands for the magnitude of the wind stress, L is the latent heat flux, H the sensible heat flux, and P the precipitation, and in which area mean a priori fluxes are affected by a star. These a priori fluxes were computed from a selection of available products to estimate each component of the heat, salt, and momentum fluxes at each grid point of the test area (see section 3.2.1). The ranges of values of the seven control parameters are given in Table 1. They were determined so as to be large enough to be sure to get the optimum, but in reasonable intervals to discard unphysical solutions.

3. Data Used and Forcings

3.1. Data and Initialization of the SCM

To implement the inverse method, the simulation test area was chosen large enough to minimize the impact of horizontal advection, but not too much so that the hydrology, water properties and bottom topography are not too heterogeneous. The area displayed in Figure 1 indicates an homogeneous bottom
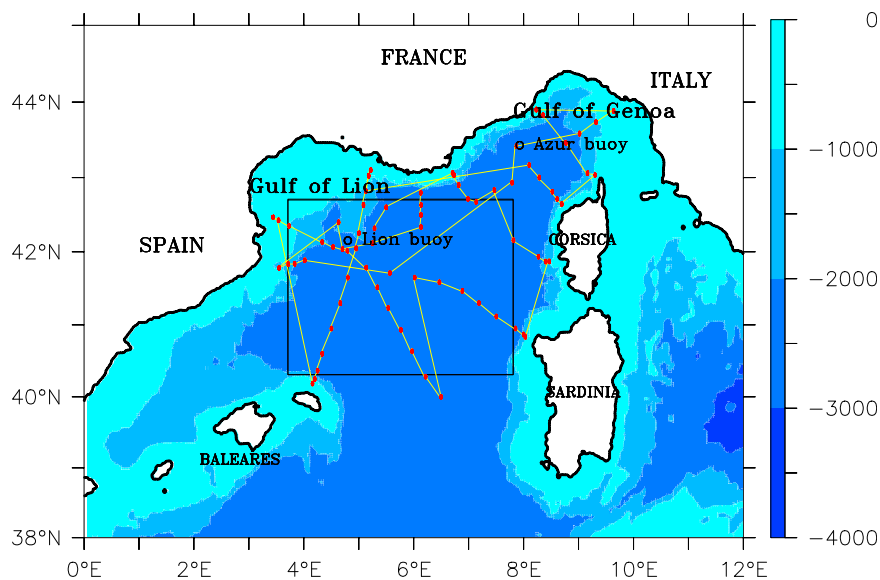
Bathymetry of the north−western Mediterranean

Figure 1. Bathymetry (m) of the north-western Mediterranean. The black box corresponds to the test area. The 89 CTDs of the MOOSE 2012 hydrological survey (from 24 July 2012 to 8 August 2012) are represented by red dots, the ship trajectory by yellow lines, and the position of the anchored AZUR and LION buoys by black circles.

topography; it includes the wintertime NWM deep convective patch [e.g., *Herrmann et al.*, 2009; *Houpert et al.*, 2016]. The simulation domain covers a surface area of about 300 × 300 km^2 but the surface flux correction can be applied on a wider area, i.e., the whole domain area represented in Figure 1.

As indicated in Figure 1, the LION buoy, anchored at 4.703°E 42.102°N, lies inside the test area, while the AZUR buoy anchored at 7.83°E 43.38°N lies in the outer domain. The LION and AZUR buoys have been providing atmospheric and oceanic observables since 2001 and 1999, respectively; these data were used for evaluation of the adjusted fluxes in section 5.1.

The inverse method was applied during one seasonal cycle from 1 August 2012 to 31 July 2013, by using most of the data collected in the test area during six hydrological surveys: MOOSE 2012 and MOOSE 2013 (respectively, from 24 July 2012 to 8 August 2012 with 89 conductivity temperature depth (CTD hereafter) casts and from 13 June 2013 to 9 July 2013 with 77 CTD casts), DeWEX-1 (from 3 February 2013 to 21 February 2013 with 75 CTD casts), and DeWEX-2 (from 5 April 2013 to 24 April 2013 with 100 CTD casts), as well as the HyMeX-SOP1 in autumn 2012 [*Ducrocq et al.*, 2014] and HyMeX-SOP2 in winter 2013 [*Estournel et al.*, 2016a]. We also used various in situ data (gliders, ARGO floats, surface drifters, moored buoys) and satellite platforms, either for initialization of the SCM (see below), or for calculating the cost function. As mentioned in the introduction, the more numerous the data, stronger is the constraint on the realism of the numerical simulations and finally on the adjusted fluxes.

During the same period, operational and research oceanic models were run and some of their outputs were used. For estimating large-scale geostrophic advections of temperature and salinity as well as horizontal Ekman advection of salinity, we used outputs of the operational MERCATOR PSY2V4R4 model [*Drillet et al.*, 2014] (see sections 3.2.2 and 3.2.3). Moreover, for evaluating the heat budget closure presented in section 5.3, the MEDRYS reanalysis [*Hamon et al.*, 2016] and some outputs of the mesoscale research SYMPHONY [*Marsaleix et al.*, 2009, 2012] and MARS3D [*Garreau et al.*, 2011] models were also used. The MEDRYS reanalysis, based on the MERCATOR assimilation system, assimilated numerous in situ data collected between 2007 and 2013 in the NWM. Unlike MERCATOR and MEDRYS, the SYMPHONY and MARS3D models do not assimilate altimetry nor in situ data. They were initialized either form MERCATOR fields (MARS3D) or from a mixed of in situ data and MERCATOR outputs (SYMPHONY) [*Estournel et al.*, 2016b] and forced with fluxes derived from NWPM fields.

The SCM was initialized with temperature and salinity profiles from 35 CTD casts collected in the test area during the MOOSE 2012 campaign (Figure 1). The temperature and salinity profiles were linearly interpolated on a
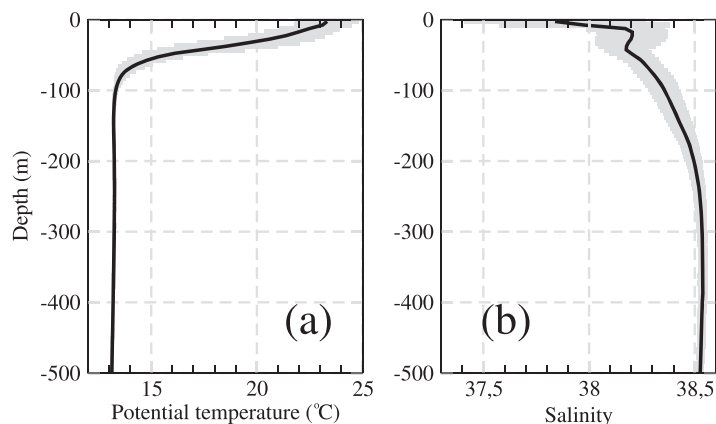
Figure 2. (a) Area mean temperature (in °C) and (b) salinity profiles from the CTDs collected within the test area (see Figure 1) during the MOOSE 2012 hydrological network with standard deviations in grey.

5 m regular vertical grid before spatial averaging (Figure 2). The profiles were used as initial state at the central time of the survey (i.e., 1 August 2012). The mean potential temperature profile (Figure 2a) is homogeneous from 2800 to 100 m due to the presence of WMDW, and covered by well-stratified surface waters above 100 m. The mean salinity values (Figure 2b) range between 38.3 and 38.6 from the bottom to about 200 m and exhibit a maximum value of 38.6 near 400 m. Above, salinity drops sharply near the surface

to 37.8. Both mean temperature and salinity profiles display substantial spatial variability near the surface, which rapidly decreases with depth (Figure 2).

3.2. Forcings

In this section, the calculation of the different terms of equation (3) forcing the SCM are detailed. Table 2 provides a list of these terms and briefly sums up the data used and their resolution.

3.2.1. Surface Fluxes

To force the SCM, a priori fluxes were computed after collecting several surface meteorological and oceanic variables. One of the objectives being to take into account oceanic mesoscales in the surface fluxes, we chose SST fields produced operationally since 2010 by the Centre de Météorologie Spatiale (Météo-France, Lannion), at a daily frequency and analyzed and positioned on a ultrahigh resolution 0.02° longitude × 0.02° latitude grid. This production is issued from the MEDSPIRATION project (http://cersat.ifremer.fr/thematic-portals/projects/medspiration) funded by the European Space Agency (ESA). The daily SSTs of the satellite analyses are foundation SSTs (i.e., the temperature free of diurnal temperature variability or the temperature upon which the growth and decay of the diurnal heating develops each day; see https://www.ghrsst.org/ghrsst-data-services/products/) and thus can be assimilated with the bulk model SSTs when comparing both series. The atmospheric variables (air temperature, humidity, sea level pressure, and surface

Table 2. List of the Various Terms of Equation (3) and Description of Data Used to Compute Them

Process	Description	Data Used	Resolution
Mean solar radiation		Satellite shortwave radiation	Hourly; 0.05° × 0.05°
Deviation from the mean solar radiation		Neglected	
Horizontal Ekman advection	Computed from equation (9)	AROME model winds, satellite SSTs and bulk algorithm [*Fairall et al.*, 2003]; MERCATOR SSSs	AROME: hourly; 0.025° × 0.025° SST: daily; 0.02° × 0.02° MERCATOR SSSs: daily; 0.05° × 0.05°
Horizontal non-Ekman advection	Geostrophy	T and S profiles from MERCATOR PSY2V4R4	Daily; 0.05° × 0.05°
Mean vertical Ekman advection	Wind stress curl and SCM <T> (and <S>) profiles	AROME model outputs and bulk algorithm [*Fairall et al.*, 2003]	Hourly; 0.025° × 0.025°
Deviation from the mean vertical Ekman advection		Neglected	
Vertical non-Ekman advection		Neglected	
Horizontal diffusion		Neglected	
Mean vertical diffusion	SCM turbulent mixing scheme. At the surface: turbulent fluxes and net longwave radiation from equation (8), precipitation	Calculated by the SCM; surface fluxes: evaluated with a bulk algorithm [*Fairall et al.*, 2003] from AROME input parameters and satellite SSTs; satellite longwave radiation; satellite precipitation (TRMM)	AROME: hourly; 0.025° × 0.025° SST: daily; 0.02° × 0.02° Longwave radiation: hourly; 0.05° × 0.05° TRMM: 3 hours; 0.125° × 0.125°
Deviation from the mean vertical diffusion	Parameterized by multiplying the wind stress by γ (subsection 3.2.5)	γ constant value (1.34) evaluated from the AROME model winds	

winds) come from the operational Météo-France AROME model [*Bouttier*, 2007]. Its outputs were available every hour on a 0.025° longitude × 0.025° latitude grid and were interpolated on the finer SST grid.

Rather than using precipitation from the AROME model, we preferred to download TRMM precipitation fields [*Huffman et al.*, 2007], because precipitating clouds or cells are better positioned than in models [*Béranger et al.*, 2006; *Pfeifroth et al.*, 2013], even if the calibration of satellite precipitation over oceans and seas can still be improved [*Serreze et al.*, 2005]. As TRMM data were available every 3 h on a 0.125° longitude × 0.125° latitude grid, the fields were linearly interpolated every hour at the resolution of the SST grid. The daily SST fields were also interpolated every hour. Finally, the COARE3.0 bulk algorithm [*Fairall et al.*, 2003] was used to produce hourly turbulent fluxes (latent and sensible heat fluxes and wind stress) on the 0.02° longitude × 0.02° latitude SST grid. No skin effects (warm and cool layer), nor second-order effects affecting the surface fluxes (corrections due to surface wave, Webb correction, sea spray, gustiness . . .) were included since the flux correction with the inverse method operates to correct the a priori fluxes, as well as these second-order effects.

The radiative fluxes (incoming longwave and shortwave radiations) were downloaded from the Centre de Météorologie Spatiale (Météo-France, Lannion), where they are produced operationally at a time frequency of 1 h on a regular grid of 0.05° longitude × 0.05° latitude [*Brisson et al.*, 1999, 2001]. These data are compared operationally with in situ measurements from on land pyranometers and pyrgeometers [*Le Borgne et al.*, 2007] and with ship data during dedicated experiments at sea [e.g., *Eymard et al.*, 1999; *Caniaux et al.*, 2005a]. Daily fluxes provide interesting comparisons with biases less than 2 W m^{-2} and root-mean-square errors ranging from 10 to 20 W m^{-2} at midlatitudes (Jordà et al., submitted manuscript, 2017). However, during the AMMA-EGEE experiment (western Africa and Gulf of Guinea in summer 2006; *Redelsperger et al.*, 2006; *Bourlès et al.*, 2007], statistics were worse, specially at hourly resolution (with root-mean-square errors of 66 and 21 W m^{-2}, respectively, for shortwave and longwave radiation) and attributed to frequent contamination by Saharan dust aerosols [*Le Borgne et al.*, 2007]. However, their good performance against in situ data at midlatitude implies that we decided not to correct them by the optimization procedure of the inverse method. Like the other flux-relative variables, the radiative fluxes were interpolated on the SST grid. The net longwave radiation F_{LW} was computed from the downwelling longwave radiation F_{DLW} and SST from the classical expression:

$$F_{LW} = (1-\alpha)F_{DLW} - \varepsilon\sigma(SST+273.16)^4 \tag{8}$$

with a longwave reflectance $\alpha = 0.045$ [*Bignami et al.*, 1995], an emissivity $\varepsilon = 0.97$, and a Stefan-Boltzmann constant $\sigma = 5.67 \times 10^{-8}$ W m^{-2} K^{-4}. For the net shortwave radiation, an albedo of 0.055 was adopted.

The mean annual surface net heat flux and wind stress are shown in Figure 3a. The area mean net heat flux is negative (-14.3 W m^{-2}), meaning cooling for the sea. Actually, the area is straddling the zero flux line located on the eastern part of the domain (thick black line in Figure 3a). The area with the lowest heat fluxes corresponds to the area of maximum wind stress associated with the dominant north-northwesterly continental winds (i.e., the northerly Mistral and north-westerly Tramontane blowing down the Rhône and Garonne river valleys). Figure 3b represents the mean annual E-P budget during the same period. The area mean value is 711 mm yr^{-1}. A belt of higher values is present to the west of the domain, where the strongest winds generate higher evaporation rate, and farther south with values up to 1000 mm yr^{-1} on the warm waters of the Balearic front. The north-eastern portion of our study region has a much lower E-P budget (∼100 mm yr^{-1}) attributable to intense precipitation, which mainly affects the Gulf of Genoa during the winter period (associated with the Genoa low located at 8°E 43°N in the NE corner of Figure 3).

3.2.2. Horizontal Ekman Advection

We assumed that the horizontal Ekman advection of temperature could be calculated from satellite SSTs and wind stress fields. This hypothesis is reasonable because the depth of the Ekman layer is relatively shallow during most time of the year in the area (Figure 4), between 35 and 50 m on average, with maximum depths in winter down to around 70 m. It is shallower and less than the mixed layer depth, so that over this depth, the temperature profiles were assumed homogeneous to be taken as SST. The horizontal Ekman advection term in equation (3) was thus computed every hour and at the same spatial scale as the surface fluxes, from the following expression [e.g., *Cushman-Roisin*, 1987]:
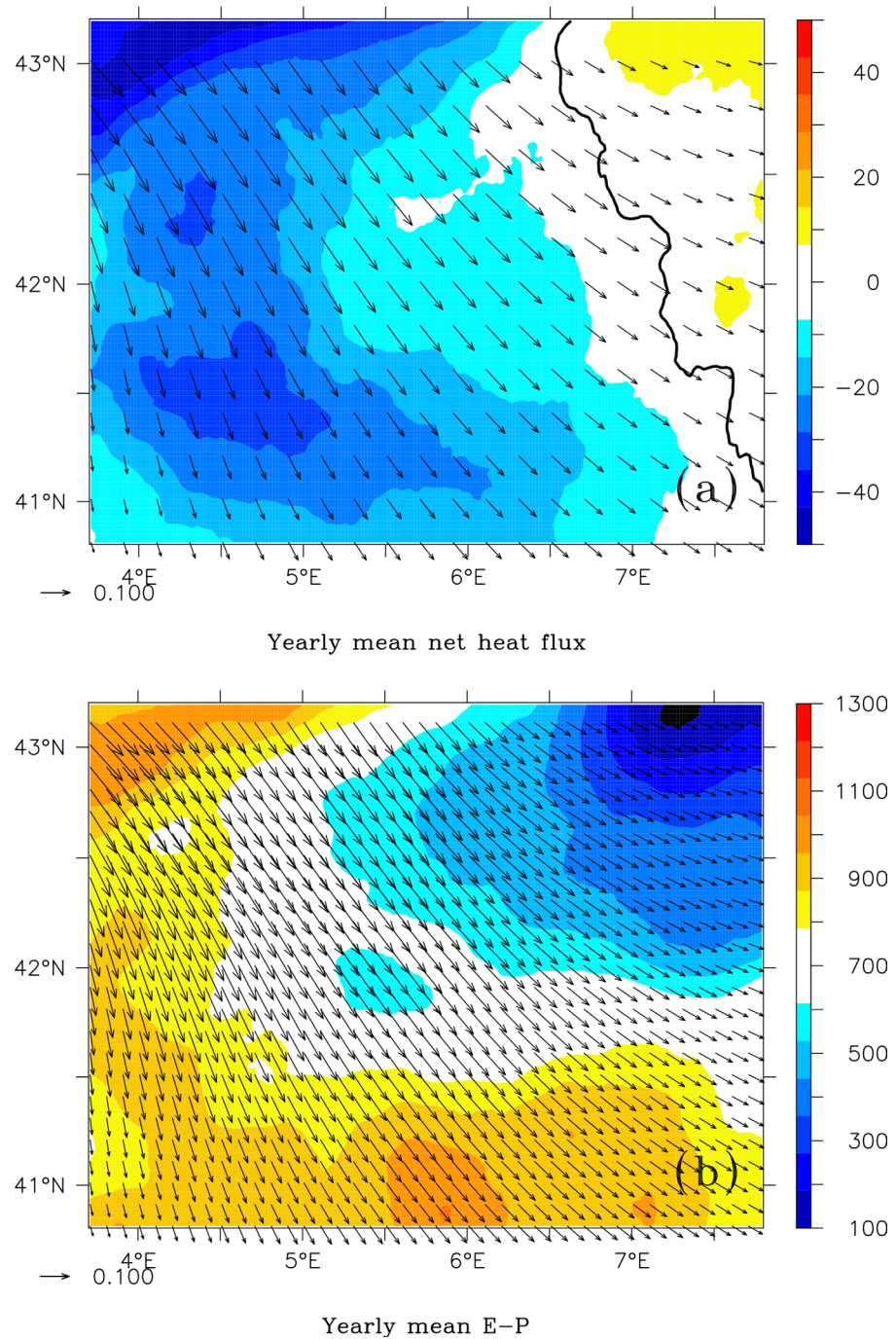
Figure 3. Map of the year mean (from 1 August 2012 to 31 July 2013) a priori fields for: (a) surface net heat fluxes (shades, units W m^{-2}) with zero isoline in black and wind stress every 10 grid points (arrows, units N m^{-2} and scale in the lower left corner); (b) evaporation minus precipitation (mm yr^{-1}) and wind stress every 5 grid points.

$$- \overrightarrow{u_e} \cdot \overrightarrow{\nabla}_h T = -\frac{1}{\rho_0 fh} \left(\overrightarrow{k} \times \overrightarrow{\tau} \right) \cdot \overrightarrow{\nabla}_h SST \tag{9}$$

where $\vec{k}$ is the unit vertical vector, $\vec{\tau}$ the wind stress and f the Coriolis parameter. According to *Cushman-Roisin* [1987], the Ekman layer depth (h) is computed from the turbulent velocity as:
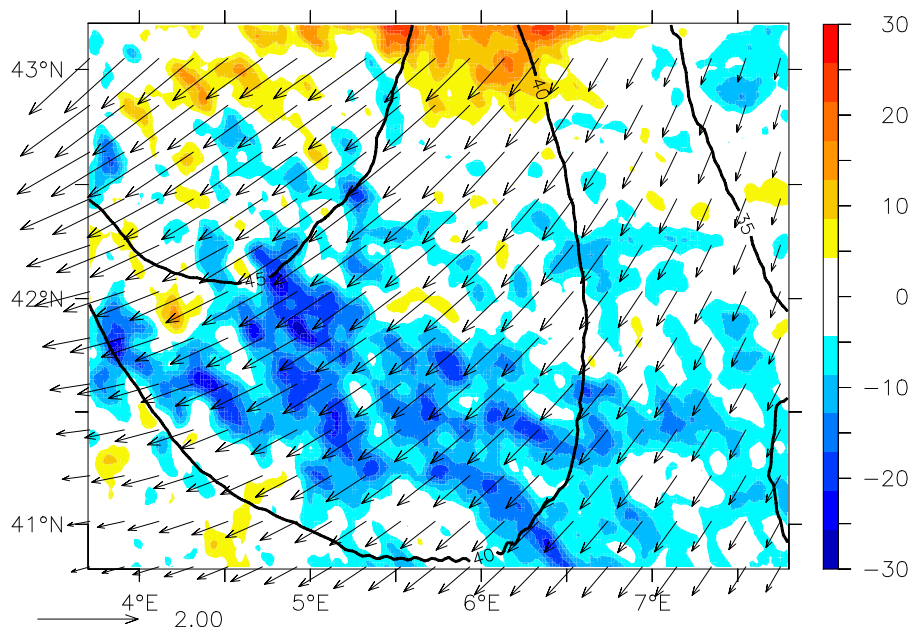
Figure 4. Same as Figure 3 for the horizontal Ekman advection of temperature (shades, units 10^{-8} °C s^{-1}), Ekman transport (arrows, units m^2 s^{-1} and scale in the lower left corner) every 10 grid points and Ekman layer depth (contours, units m).

$$h = 0.4 \frac{u_*}{f} \qquad (10)$$

with $u_* = \sqrt{\frac{\tau}{\rho_0}}$. A similar formulation was used for the horizontal Ekman advection of salinity, in which the SSS values were taken from the MERCATOR PSY2V4R4 model and linearly interpolated every hours on the same spatial grid as SSTs. In the SCM, horizontal Ekman advection was added as an external forcing term on the thickness of the Ekman layer h.

Figure 4 represents the mean annual horizontal Ekman advection of temperature, superimposed with the Ekman transport and Ekman layer depth. Over the whole area, the Ekman transport is south westward, perpendicular to the dominant surface wind stress. The mean annual transport of temperature has predominantly positive values in the north (i.e., warming) and negative values in the south. This configuration, far from reflecting the mean transport of the time mean SST field by the time mean current, reflects the important role of the eddy field (not shown). The mean annual depth of the Ekman layer, with values ranging from 35 to 50 m, is deeper in the north-western part of the domain due to the influence of the dominant winds.

3.2.3. Horizontal Non-Ekman Advection

For the horizontal non-Ekman advection (term $-\langle \vec{u}_{ne} \cdot \vec{\nabla}_h T \rangle$ in equation (3)), we used geostrophic advections derived from the MERCATOR PSY2V4R4 model. This model assimilates altimetry, assuming that the large-scale circulation in the NWM is better constrained than in models without assimilation. Moreover, many comparisons were done with MARS3D and SYMPHONIE models and with MEDRYS reanalysis during winter 2012–2013 in the NWM (not shown). These comparisons led us to conclude that the MERCATOR model responds quite well to our needs for reconstructing geostrophic advections over the whole water column.

The seasonal time-depth evolution of the mean temperature geostrophic advection is presented in Figure 5. The plot confirms that advections are the strongest in the surface layers down to a depth of about 150 m. From January to March, geostrophic advections were weaker than during the rest of the year because during this period intense cooling significantly reduced horizontal gradients of temperature and salinity across the area, despite the intensification of the rim-current. During the rest of the year, alternatively warm and cold subsurface advections reflect the presence of mesoscale features (eddies and filaments) mainly transiting along the Balearic front around 40°N. At the surface and after one annual cycle, geostrophic advection tends to warm SSTs and freshen SSSs in the test area.
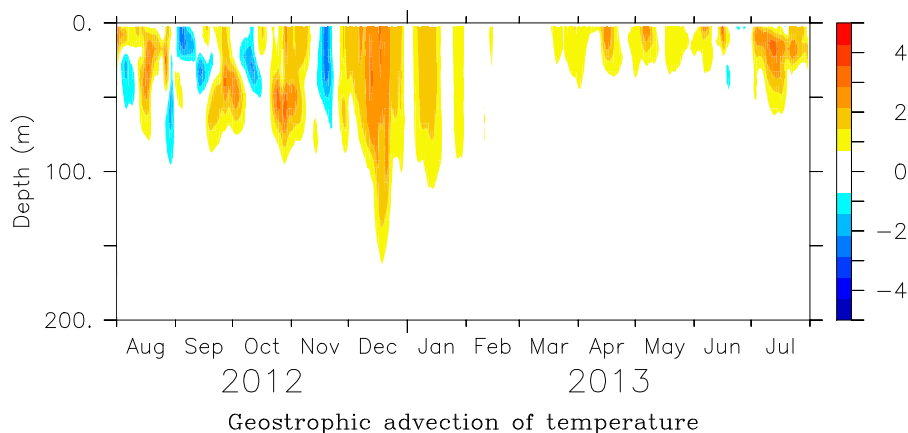
Figure 5. Temporal evolution of the domain average geostrophic advection of temperature (10^{-7}°C s^{-1}) as a function of depth (m).

3.2.4. Vertical Ekman Advection

At any point of the test area and at each time step, a vertical Ekman velocity w_e was evaluated from the wind-stress curl and then averaged over the test area. For computing vertical Ekman advections of temperature and salinity (term $-\langle w_e \rangle \partial_z \langle T \rangle$ in equation (3)), a vertical profile for $<w_e>$ must be prescribed. As in *Caniaux et al.* [2005b], we chose zero at the surface, maximum or minimum (according to the sign of the vertical velocity) at the Ekman layer depth h, and decreasing linearly to zero at the bottom of the water column. In the SCM, vertical Ekman advections were calculated at each level of the model from vertical gradients of temperature and salinity and from the vertical profile of $<w_e>$ with an upstream numerical scheme compatible with the other schemes of the model.

The mean annual Ekman pumping is displayed in Figure 6. An ascending positive (subsiding negative) pumping zone is present on the left cyclonic (right anticyclonic) side of dominant winds. The two areas of opposite sign are separated by a nearly 110 km wide corridor corresponding to the main pathway of the dominant winds in the area. Note that the patterns of higher and lower pumping values are consistent with
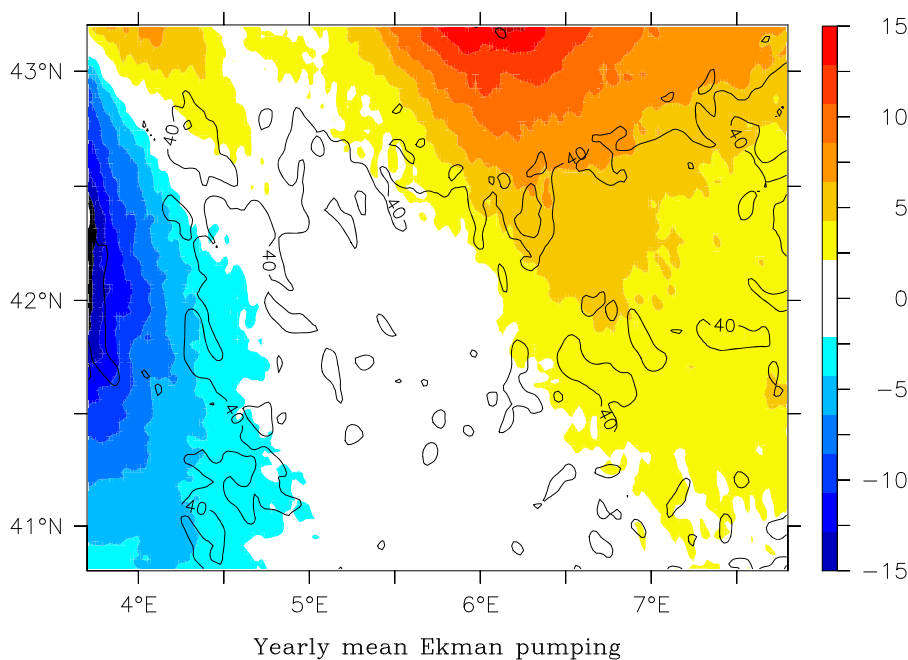

Figure 6. Same as Figure 3 for the Ekman pumping (shades, units 10^{-6} m s^{-1}) and temporal standard deviation (contours, units 10^{-6} m s^{-1}). Contour intervals are 40×10^{-6} m s^{-1}.

the patterns of a high temporal variability (yearly standard deviations $> 40 \times 10^{-6}$ m s^{-1}, i.e., 3 times the values of the signal, due to the frequent gale force winds alternating with frequent calm weather conditions). The north-eastern area with positive pumping plays an important role for preconditioning water masses, by maintaining the doming of isopycnals inside the gyre interior, as underlined by *Gascard* [1978] and *Madec et al.* [1996] in the Gulf of Lion or by *Pickart et al.* [2003] in the Irminger Sea, where the Greenland tip jets generate elevated heat loss and strong wind stress curl in the lee of Cape Farewell. As the magnitude of the positive wind stress curl and its extension are larger than that of the negative pumping zone, a mean annual positive value is expected in the test area.

3.2.5. Subgrid-Scale Vertical Mixing

This term, symbolized in equation (3) by the expression $\partial_z \langle K'' \partial_z T'' \rangle$, represents a physical process difficult to estimate and poorly documented in the literature. As in *Caniaux et al.* [2005b], we have assumed that this term tends to increase the vertical mixing simulated by the SCM. We thus assumed that this additional contribution to vertical mixing was due to spatial heterogeneities in the wind field throughout the test area. To parameterize this subgrid-scale process, we considered that the wind stress was increased by a factor taking into account the spatial standard deviation σ_W of the wind magnitude W, i.e., by multiplying the wind stress by the factor $\gamma = 1 + \frac{\sigma_W}{U}$. All year long, the time series of the wind W, of σ_W and finally of γ display a high-frequency variability but with no significant trend (not shown). Consequently, a constant value for this factor was specified and taken equal to its mean annual value ($\gamma = 1.34$).

3.2.6. Other Terms

The vertical non-Ekman advection term, as well as the deviation term of the vertical Ekman advection in equation (3) are several order of magnitude less than vertical Ekman advection, meaning that averaged over the test area these terms can be reasonably neglected. The deviation term in the solar radiation can also be neglected since no observational evidence of any spatial correlation exists between irradiance and the pigment-dependent solar penetration in the NWM [*Simonot and Le Treut*, 1986]. The order of magnitude of the horizontal diffusion term in equation (3) can be estimated from the literature. In a realistic mesoscale simulation of the north-east Atlantic, *Caniaux and Planton* [1998] estimated horizontal diffusion of the order of 3% of the mixed layer heat budget. In a mesoscale simulation of the tropical Pacific during the TOGA/COARE experiment, *Dourado and Caniaux* [2001] found that horizontal diffusion represented a cooling less than 2 W m^{-2} or 2% of a heat storage term. Other heat balance studies, performed from data in the same basin and during the same experiment found this term negligible compared to the other mixed layer processes [*Cronin and McPhaden*, 1998; *Smyth et al.*, 1996; *Feng et al.*, 1998]. Consequently in our study, we assume that the area mean horizontal diffusion term represents 1 or 2% of the heat balance and is thus neglected (Table 2).

4. Results

4.1. Adjusted Control Parameters

The optimization with the genetic algorithm was performed after running 50,000 simulations of the SCM during one annual cycle. For each simulation, the control parameters were chosen by the genetic algorithm in their preselected range of values (Table 1) and the cost function computed. In Figure 7, the fitness function (10,000 times the inverse of the cost function) is plotted against the value of each control parameter. Each black point corresponds to the fitness value evaluated for each simulation and the red circle is the maximum fitness function. The latter provides the optimal set of control parameters, which also figure in Table 1.

The optima for R and d_2 (Table 1 and Figures 7a and 7b) are close to the values in *Jerlov*'s [1976] classification, although R appears slightly undervalued compared to type III waters. However, the adjusted values represent a mean annual value for different water types, which may change during the year and through the area. In Figure 7, sharp peaks of the fitness function correspond to well-identified optimum values. This is the case for the wind coefficient β_w (Figure 7c) and the latent heat flux coefficient β_l (Figure 7e). Conversely, the sensitivity of the simulations to the control parameters is lower for the sensible heat flux coefficient β_h (Figure 7f) and for the precipitation coefficient β_p (Figure 7g) for which the values of the fitness function form almost a plateau.

In Table 1, the optimum of β_w means that the wind needed to be slightly increased by a factor of 1.066, for optimizing both the wind stress, the latent (as well as evaporation) and sensible heat fluxes, the horizontal
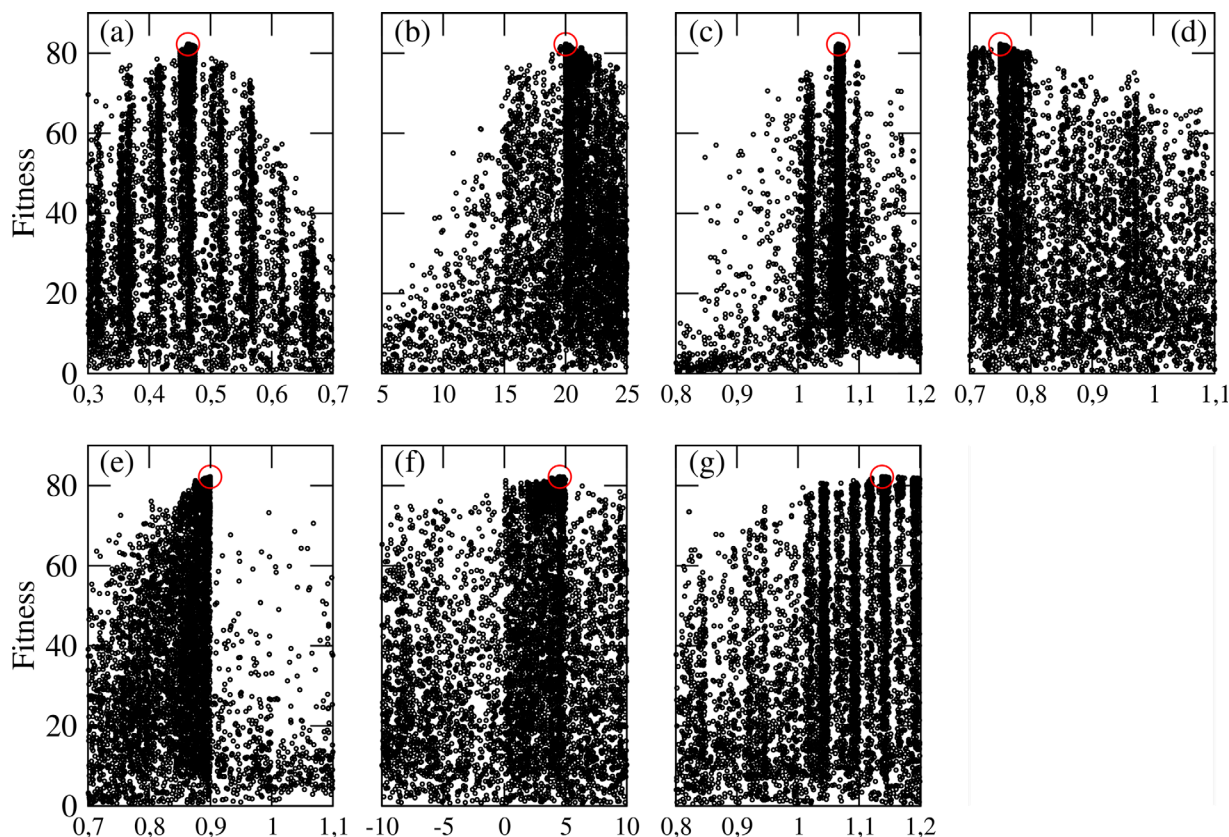
Figure 7. Fitness function for each control parameter: (a) R, (b) d$_2$, (c) β_w, (d) β_{ws}, (e) β_l, (f) β_h, and (g) β_p. The maximum fitness values are circled.

and vertical Ekman advections. On the other side, the optimum of β_{ws} (supposed to correct the exchange coefficient of the wind stress) being 0.75 means that the a priori wind stress was largely overestimated and according to equation (7) had to be reduced by a final factor of $0.75 \times 1.066^2 = 0.85$. Similarly, the exchange coefficient of the latent heat flux had to be multiplied by a factor of 0.9 and the a priori flux by a factor of $0.9 \times 1.066 = 0.96$. Note that the TRMM precipitation fields were underestimated by a factor of 1.138 for adjusting the model near-surface salinity. Accordingly, when the flux correction is applied to each grid point of the test area with equation (7), and during one annual cycle the mean latent and sensible heat fluxes were increased by 4.7 and 3.5 W m^{-2}, respectively (Table 3); this led to an increase of the net heat flux by 8.2 W m^{-2}. Similarly, the adjusted E-P balance is reduced by 163 mm yr^{-1}, due to an overestimation of evaporation (60 mm yr^{-1}) and an underestimation of a priori precipitation (103 mm yr^{-1}). The average value of the adjusted wind stress is lowered by about 0.02 N m^{-2}.

4.2. The Optimized Simulation

We now compare the evolution of the area mean satellite SST, reanalyzed SSS and residual buoyancy evolutions (considered as our reference) with the model simulations after introducing successively the three advection terms (geostrophic advection, horizontal Ekman advection, vertical Ekman advection), then the surface fluxes and finally the adjusted surface fluxes. Figure 8 displays the contribution and order of magnitude of each process

Table 3. Comparison of A Priori and Adjusted Mean Annual Fluxes[a]

Flux	A Priori	Adjusted	Difference
Sensible heat flux (W m^{-2})	−16.4	−12.9	−3.5
Latent heat flux (W m^{-2})	−113.8	−109.1	−4.7
Net heat flux (W m^{-2})	−14.3	−6.1	−8.2
Wind stress (N m^{-2})	0.156	0.133	0.023
Evaporation (mm yr^{-1})	1460.8	1400.9	59.9
Precipitation (mm yr^{-1})	749.3	852.3	−103.0
Evaporation-Precipitation (mm yr^{-1})	711.5	548.6	162.9

[a]Domain considered: 3.71°E–7.79°E to 40.31°N–42.69°N; period considered: 1 August 2012 to 31 July 2013.

Figure 8. Temporal evolution of (a) SST (°C), (b) SSS, and (c) residual buoyancy (m² s⁻²) simulated by the model, when activating only geostrophic advection (dark green curve), then successively adding horizontal Ekman advection (green), vertical Ekman advection (cyan), surface fluxes (orange), and when using the adjusted surface fluxes (red curve). The black curves correspond to the reference (a) mean satellite SSTs, (b) analyzed SSSs from in situ data during the period 9 January 2013 to 7 May 2013, and (c) residual buoyancy (computed from the 3-D analyses during the same period). The black points correspond to the residual buoyancy calculated from the CTDs collected in the test area during MOOSE 2012 (median date 1 August 2012), DeWEX-1 (13 February 2013), DeWEX-2 (14 April 2013), and MOOSE 2013 (29 June 2013).

during one annual cycle and how the simulations of SST, SSS, and residual buoyancy are improved with the adjusted fluxes.

Satellite SSTs present a significant seasonal cycle with a peak to peak amplitude of 15°C (black curve in Figure 8a). The annual cycle is flattened in winter because SSTs never fall below 12.8°C when the mixed layer is deep. Some marked cooling events punctuated the seasonal cycle in autumn (e.g., in early December) and some warming events in spring (e.g., mid-April and mid-June) in response to intense surface fluxes. After introducing geostrophic advection alone (dark green curve in Figure 8a), the modeled SST series is marked by a regular warming with a final yearly gain of 2.6°C. When adding horizontal Ekman advection (green curve in Figure 8a), the SST trend drops to about 1.5°C, while with vertical Ekman advection (cyan curve) the yearly trend decreases. Obviously, the surface flux allows to reconstruct the annual cycle and the intra seasonal warming and cooling short events (orange curve in Figure 8a). Remarkably, the modeled SST series obtained with the adjusted fluxes (red curve) is quite close to the daily satellite SST series, with a bias of 0.011°C (0.06%) and a mean standard deviation of the differences between the two series of 0.32°C.

An estimate of the uncertainty on the simulated SST series may be obtained. By assuming an expected error of 5% on the minimum of the cost function (*Sumata et al.* [2013] estimates that the error is function of the number of generations prescribed for the genetic algorithm and that the error falls to 0.5% after 1000 generations; here 500 generations were prescribed, such that a 5% error adopted here may be considered as a rather large value), an uncertainty on each optimized control parameter may be deduced from Figure 7. After running 2 *M* (i.e., 14) SCM simulations with each optimum control parameter ± one uncertainty value, and by taking the standard error of the 2 *M* simulated SST biases, the uncertainty on the bias is 0.072°C.

For SSSs, our reference is the analyzed wintertime series (see section 2.2). SSS values range from 38.04 to 38.36 with a maximum reached in late February 2013 (black curve in Figure 8b). By introducing geostrophic advection, SSS undergoes a strong but quite steady decrease of 1.2 unit after 1 year (dark green curve in Figure 8b). Horizontal Ekman advection reduces the yearly trend and introduces seasonal variability in autumn and winter (green curve). Vertical Ekman advection generates higher-salinity values associated with an import of salinity from depth and helps to further reduce the negative trend (cyan curve in Figure 8b).

With the a priori fluxes, the annual range of SSS drops significantly (orange curve in Figure 8b). Finally, with the adjusted fluxes (red curve in Figure 8b), the daily wintertime difference with the analyses falls to 0.011 (0.03%) and the standard deviation of the differences between the series to 0.04. Some brief events, that cause sudden SSS drop (e.g., late March and late April), were associated with substantial rainfall. These events are less well reconstructed in the analyses compared to those simulated by the SCM. The source of this discrepancy certainly relies in the smoothing effect of the analyses inherent to the optimal interpolation technique used. Note that during the simulation period, SSSs exhibit an overall insignificant negative trend due to the quasi-balance between the surface fluxes and the advection terms, despite a positive input of salinity in January associated with a positive horizontal Ekman advection. A similar computation of the uncertainty as for SSTs, provide an uncertainty of 0.008 for the modeled SSSs.

The residual buoyancy was evaluated from the wintertime daily temperature and salinity analyses, as well as from CTDs of the four hydrological networks (black curve and black dots in Figure 8c). The residual buoyancy rapidly decreases from mid-January 2013 and reaches a minimum at the end of February, when the surface area occupied by low stratified waters presents its maximum extension in the test area, after which the residual buoyancy increases during the spring restratification. Geostrophic advection (dark green curve in Figure 8c) produces a marked residual buoyancy increase up to 1 m^2 s^{-2} after 1 year. The effect of horizontal Ekman advection is to reduce the trend (green curve). Added to horizontal advection, vertical Ekman advection results in the destratification of the water column in winter and restratification in spring (cyan curve). After introducing the surface fluxes, the peak to peak annual cycle is enhanced (orange curve in Figure 8c). Finally, the effect of the adjusted fluxes is striking: the bias between the model and analyzed series falls to -0.029 m^2 s^{-2} and the standard deviation of the differences to 0.05 m^2 s^{-2}. This has the effect of producing a fairly good agreement with the values of the reanalyzed MOOSE 2013 network (red curve) after almost one seasonal cycle. For the residual buoyancy, the uncertainty is 0.012 m^2 s^{-2}.

5. Evaluation

5.1. Comparison With Fluxes at the LION and AZUR Buoys

The adjusted fluxes were calculated over a larger area than the test area (0°E–12°E, 38°N–44.5°N; see Figure 1), i.e., the simulation domain of the operational Météo-France AROME model over the Mediterranean Sea. However, the spatial resolution was reduced to a grid of 0.04° longitude × 0.04° latitude to avoid spatial interpolations near the coast. The calculation was performed by applying equation (7) at each grid point of the large domain area, every hour and during 1 year (1 August 2012 to 31 July 2013).

In this section, we evaluated the adjusted fluxes locally, through their comparison with the in situ data collected at the LION and AZUR buoys (see locations in Figure 1). The buoy data sets include radiative fluxes (incoming longwave and shortwave radiations) and all the near-surface meteorological observables needed to estimate the turbulent fluxes, except precipitation. Previously, the variables downloaded from the HyMeX website were scrupulously checked. Out-of-range values were cleaned and sequence values deemed to be unreliable or displaying periods of constant values were rejected. The data were then placed on a regular, hourly temporal grid, and isolated missing data or short sequences of missing data were linearly interpolated from adjacent ones. Compatibility between relative humidity and dew-point measurements was checked and corrected if necessary (for example, dew-point values could excess air temperatures, under high humidity or saturated conditions). Finally, because of missing sequences and rejected data, only 1818 and 514 hourly fluxes (over 8760) were available at the LION and AZUR buoys, respectively, for the comparison.

One must keep in mind that expected statistical errors on the net heat fluxes estimated at the LION and AZUR buoys may not be negligible. An estimate of the errors obtained by taking the errors of the observations as well as the mean values of the observables and fluxes estimated with the COARE3.0 bulk algorithm for the period 2012–2013 at the LION buoy is presented by Jordà et al. (submitted manuscript, 2017). The calculation led to errors on the net heat flux of 15 W m^{-2}, a figure close to those reported by *Colbo and Weller* [2009] in the subtropics or by *Cronin et al.* [2014] for the tropical Pacific. When the bulk algorithm error is considered in the calculation, the total error rises to 21 W m^{-2}. This is the reason why, for comparing the adjusted and the buoy net heat fluxes, we preferred to use several bulk algorithms instead of selecting only one, due to errors affecting bulk formulae. For that, we selected seven bulk formulae, established over various oceanic basins of the world ocean, i.e., *Anderson* [1993], *Brut et al.* [2005], *Fairall et al.* [2003], *Dupuis*
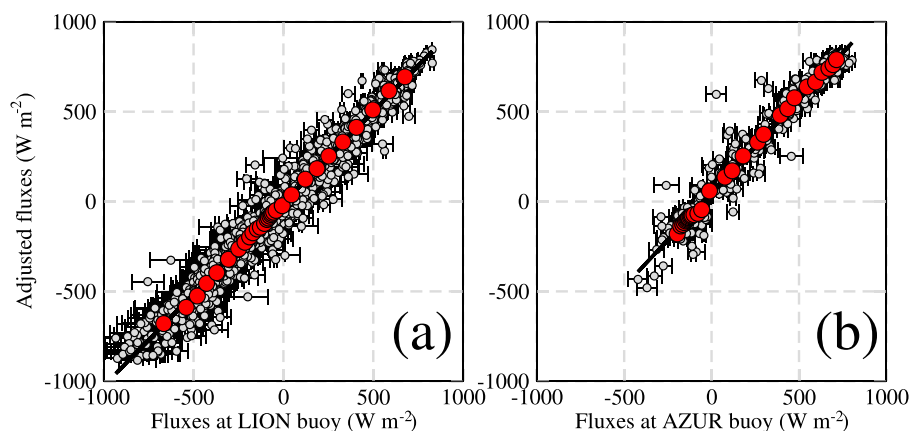
Figure 9. Scatterplot (grey points) and Q-Q (red points for the 30-quantiles) plot comparing the adjusted fluxes with the surface net heat fluxes estimated from in situ measurements: (a) at the LION (N = 1818; r^2 = 0.96) and (b) AZUR buoys (N = 514; r^2 = 0.96). The turbulent fluxes were evaluated with seven bulk formulae and the medians of the seven estimates are plotted with their inter-quartile range represented by horizontal bars. The comparison covers the period 1 August 2012 to 31 July 2013.

et al. [2003], *Persson et al.* [2005], *Caniaux et al.* [2005a], as well as *Smith* [1980], whose wind stress parameterization was associated with *DeCosmo et al.* [1996] for the latent and sensible heat fluxes. Figure 9 represents the scatter plots at the two buoys of the adjusted net heat flux series versus the median of the seven net heat flux estimates, as well as their inter-quartile range (IQR hereafter).

The net heat flux at the buoys is predominantly governed by turbulent heat flux and solar radiation and its sign depends on the seasonal balance between net solar radiation and latent heat flux. At the LION buoy (Figure 9a), the range of the net heat flux is much larger ($\sim$1700 W m^{-2}) than at the AZUR buoy ($\sim$1200 W m^{-2}; Figure 9b), a consequence of limited sampling at AZUR buoy, and in part because the LION buoy is located on the passage of prevailing stronger winds with frequent intrusions of cold and dry air from the north. The adjusted and the median of the in situ fluxes are in fair agreement (r^2 = 0.96 at the two buoys), with only a weak spread of the data around the first diagonal of the diagram. Note that the IQR of the medians at the two buoys are much more important at low (negative) than at high (positive) flux values, due to greater uncertainties in the turbulent heat flux exchange coefficients at high wind, and large contrast of temperature and humidity between the air and the sea surface. Despite the statistical errors reported above on the net heat fluxes at the LION buoy, the agreement of the buoys and adjusted fluxes remains fairly good over the whole range of values with no skew, even for low or high fluxes, as indicated by the thirtieth quantiles of the Q-Q plot (red dots in Figure 9).

5.2. Evaluation of Numerical Weather Prediction Model (NWPM) Fluxes

In this section, we compare the adjusted fluxes, considered as a reference, with fluxes of four operational numerical weather prediction models (NWPM): the French ARPEGE [*Courtier et al.*, 1991] and AROME [*Bouttier*, 2007] models, the NCEP and ECMWF models and one reanalysis, ERA-INTERIM [*Dee et al.*, 2011]. The fluxes of the five products were linearly interpolated on the same horizontal grid (0.02° × 0.02°) as the adjusted fluxes and compared over the test area. Table 4 provides mean annual values of the individual flux components of the net heat and water fluxes, as well as the wind stress, along with the standard deviations.

All model products display a net heat loss for the sea, but they all underestimate the adjusted fluxes, sometimes dramatically like ARPEGE (the difference reaches 46 W m^{-2}), others weaker like ERA-INTERIM (8 W m^{-2}). Note the substantial dispersion between the NWPM products with a more than twofold intervariation (the range, 38 W m^{-2}, is of the same order of magnitude as the median, -25 W m^{-2}). The model products differ from the adjusted fluxes for different reasons. The differences are primarily the result of differences in either the sensible heat flux for AROME and ARPEGE (the heat loss exceeds $+10$ W m^{-2}), in the latent heat flux for ARPEGE (<-15 W m^{-2}) and ERA-INTERIM ($>+10$ W m^{-2}), in the net longwave radiation for the ECMWF and AROME (<-13 W m^{-2}), or in the net shortwave radiation for the NCEP ($>+10$ W m^{-2}). On average, the NECP and ERA-INTERIM underestimate the adjusted wind stress by 0.028 and 0.016 N m^{-2}, respectively, while the other products overestimate the adjusted wind stress over 0.01 N m^{-2}.

Table 4. Comparison of the Operational NWPM: ARPEGE, AROME, NCEP, ECMWF, and of the ERA-INTERIM Reanalysis With the Adjusted Fluxes[a]

Flux	ARPEGE	AROME	NCEP	ECMWF	ERA-INTERIM	Adjusted
Sensible heat flux (W m^{-2})	−23.2 (56.3)	−27.0 (64.3)	−21.4 (55.3)	−17.7 (38.6)	−16.2 (37.2)	−12.9 (34.9)
Latent heat flux (W m^{-2})	−124.7 (152.8)	−109.0 (127.5)	−118.6 (143.8)	−109.5 (117.8)	−98.9 (105.9)	−109.1 (114.5)
Net longwave W m^{-2})	−76.9 (23.8)	−79.6 (22.8)	−77.4 (23.0)	−80.5 (20.5)	−79.0 (21.1)	−66.3 (17.2)
Net shortwave (W m^{-2})	+172.7 (216.4)	+190.7 (223.2)	+192.7 (228.9)	+184.5 (221.0)	+179.8 (219.1)	+182.2 (266.7)
Net heat flux (W m^{-2})	−52.1 (317.2)	−24.9 (311.1)	−24.7 (327.0)	−23.2 (284.0)	−14.3 (274.3)	−6.1 (319.4)
Wind stress (N m^{-2})	0.143 (0.189)	0.149 (0.202)	0.105 (0.145)	0.145 (0.188)	0.117 (0.148)	0.133 (0.167)
Evaporation (mm yr^{-1})	1599.8 (1962.1)	1398.7 (1632.5)	1456.4 (1772.4)	1380.9 (1485.5)	1247.5 (1335.4)	1400.9 (1468.5)
Precipitation (mm yr^{-1})	727.9 (1988.0)	688.1 (2317.4)	731.0 (2098.0)	685.6 (1861.9)	654.6 (1833.0)	852.3 (2851.4)
Evaporation-precipitation (mm yr^{-1})	871.9 (2625.8)	710.6 (2770.0)	725.4 (2550.5)	695.3 (2280.3)	592.9 (2237.8)	548.6 (3133.5)

[a]Standard deviation values in parenthesis. Domain considered: 3.71°E–7.79°E to 40.31°N–42.69°N; period considered: 1 August 2012 to 31 July 2013.

The model E-P budgets display a high dispersion (Table 4). Moreover, all NWPM overestimate the adjusted water budget, sometimes radically, with ARPEGE exhibiting the greatest difference with the adjusted fluxes (323 mm yr^{-1}). Again, ERA-INTERIM is the model that most agrees with the adjusted fluxes (44 mm yr^{-1}), certainly a consequence of a greater amount of data assimilated in the reanalysis. This behavior results from differences in evaporation and from systematic and substantial underestimate of precipitation by the NWPM (the difference with the model mean is −155 mm yr^{-1}). All model products underestimate the uncorrected TRMM precipitation as well (not shown). A similar conclusion was reached by *Alhammoud et al.* [2014] who noted that rainfall and specially convective rainfall in ERA-INTERIM over the Mediterranean Sea were systematically underestimated compared to microwave satellite retrievals. The large dispersion between NWPM, both for heat and water fluxes, suggest the importance of errors and drift affecting model runs, when ocean models are forced with atmospheric NWPM flux fields without any correction [e.g., *Sanchez-Gomez et al.*, 2011; *Valdivieso et al.*, 2015]. Surprisingly, all the model products appreciably underestimate the variability of the satellite shortwave radiation (Table 4) as well as the variability of satellite precipitation compared with the adjusted ones (Table 4) and even with uncorrected TRMM fields (not shown). Consequently, the variability of the E-P budget is also underestimated by all the model products.

Figures 10 and 11 compare the mean annual adjusted flux fields over the larger domain with ARPEGE and ERA-INTERIM fields, respectively, the farthest and closest models in comparison with the adjusted fluxes. The spatial patterns of the annual net heat flux (Figure 10) are similar, with heat loss between the Gulf of Lion and Sardinia, reflecting the dominant wind pattern, in the Gulf of Genoa and east of Sardinia. The maximum heat loss (∼−60 W m^{-2}) is located in the Gulf of Lion, along the continental margin (Figure 10a). A belt of positive values (heat gain for the ocean of about 10–20 W m^{-2}) extends between the southern Pyrenees, the Balearic islands and along the Sardinia and Corsica islands. In both models, the amplitudes differ considerably with the adjusted fluxes with differences reaching locally up to 60 W m^{-2}. In ARPEGE, the zero flux line is hardly present in the vicinity of the Balearic Islands (Figure 10b), while in ERA-INTERIM (Figure 10c) the zero flux line delimits a much larger surface area than in the adjusted fluxes.

For the water fluxes (Figure 11), the spatial pattern of the adjusted fluxes displays higher values in the Gulf of Lion and from the Balearic to Sardinia islands (750–1000 mm yr^{-1}) and much lower values in the Gulf of Genoa, with an excess of precipitation over evaporation rates (Figure 11a). The flux fields of the two models present the same longitudinal gradient pattern but with less mesoscale features than the adjusted fluxes (Figures 11b and 11c), like in the net heat flux fields. The absence of mesoscale features in the NWPM mean annual heat and water flux fields results from the coarser spatial resolution of SST fields used in NWPM. Actually, most of them use the 6 km resolution OSTIA analysis [*Donlon et al.*, 2012] which is derived from coarser resolution (mostly satellite) products, which alter the SST and thus the flux mesoscales, compared to the ∼4 km resolution of our flux retrievals based on the ∼2 km resolution SST product. The ARPEGE model presents an obvious excess of evaporation and stronger wind stress from the Gulf of Lion to southern Sardinia, while the region of rainfall excess in the Gulf of Genoa is unrealistically underestimated (Figure 11b).
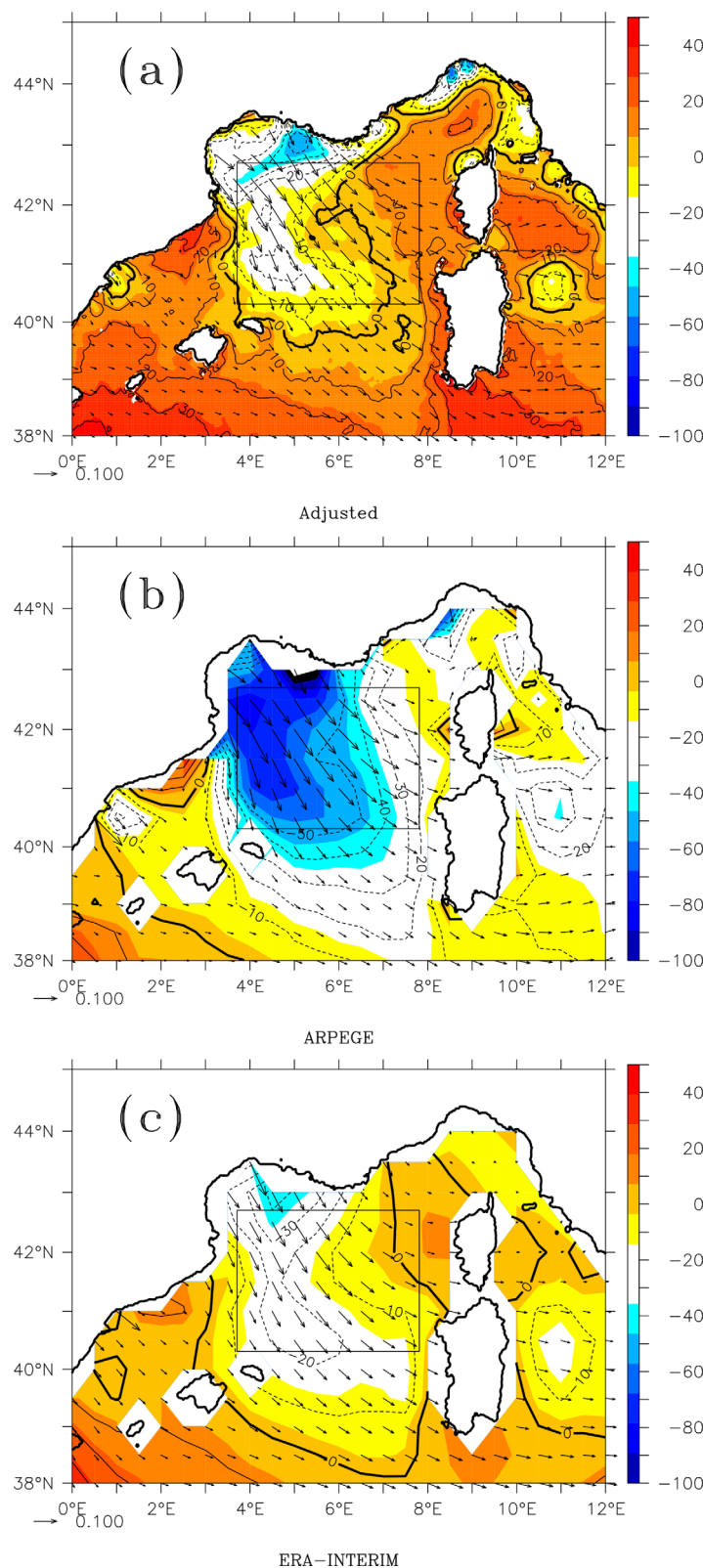
Figure 10. Maps of the annual net heat flux (shades, W m^{-2}) and wind stress (arrows, N m^{-2} and scale in the lower left corner) for (a) the adjusted flux data set, (b) the ARPEGE model, and (c) ERA-INTERIM. Period considered: 1 August 2012 to 31 July 2013. Contour intervals are 10 W m^{-2}. The wind stress is represented every 10 grid points.

5.3. Evaluation of the Heat and Water Budget Closure

The objective of this section is to show how the fluxes deduced from the inverse method allows to close the heat and water budgets. A heat budget throughout the water column was performed on the test area between MOOSE 2012 and MOOSE 2013 surveys separated by 333 days. The tendency, surface flux, geostrophic and Ekman advections and a residual were calculated independently, either from in situ data, or from objective analyses of the CTD networks, or from the ocean models, which were run between the two MOOSE networks. The ocean models include the MERCATOR PSY2V4R4 model, the MEDRYS reanalysis, and the mesoscale models SYMPHONY and MARS3D, as well as the SCM forced with the adjusted fluxes.

The terms of the heat and water budgets were computed as box and whisker plots to highlight their contribution and spread (Figure 12). The tendency term was calculated from seven different ways: from the mean CTDs collected in the test area during MOOSE 2012 and MOOSE 2013, as well as from objectively analyzed fields deduced from the two hydrological surveys. The 3-D analyzed fields were produced exactly like the wintertime surface temperature and salinity analyses (see section 2.2), except that they only include survey CTDs [*Giordani et al.*, 2014]. Other tendency term estimates were provided by the ocean 3-D models (MERCATOR, SYMPHONY, and MARS), the MEDRYS reanalysis and the SCM. The seven estimates of the tendency term are reported in the first column of Figure 12a. The median is negative, meaning cooling for the water column (-16 W m^{-2} with an IQR of 6 W
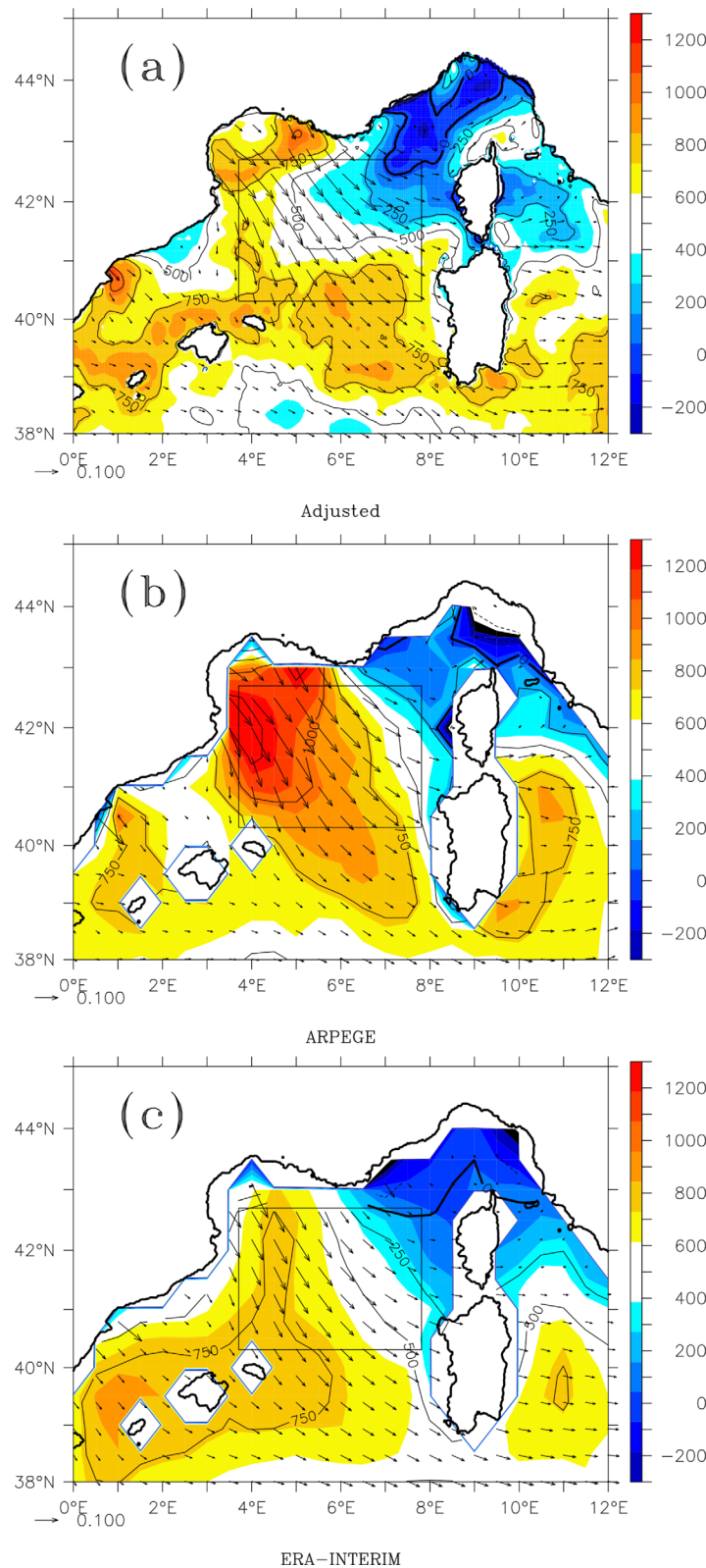
Figure 11. Same as Figure 10 for the net water flux in mm yr^{-1}. Contour intervals are 250 mm yr^{-1}.

m^{-2}). For getting more than one estimate of the adjusted fluxes, four optimization experiments were performed, wherein only geostrophic advection was changed (i.e., the MERCATOR geostrophic advection was replaced by the SYMPHONY, MARS3D and MEDRYS ones), because this term is one of the main sensitive terms and source of errors in the flux retrieval. For these four estimates (second column of Figure 12a), the median is -21 W m^{-2} (IQR $= 12$ W m^{-2}), which again means cooling for the ocean.

In the third column of Figure 12a, the surface fluxes of the five NWPM presented and evaluated in the previous sections are reported. The negative median (-44 W m^{-2}), almost twice the median of the adjusted fluxes and the large spread between model fluxes (IQR $= 23$ W m^{-2}, twice the IQR of the adjusted fluxes) are in agreement with the conclusions of the previous section. The total advection terms (column 4 of Figure 12a), i.e., the sum of horizontal geostrophic advection, horizontal and vertical Ekman advections (represented, respectively, in columns 5, 6, and 7), were estimated with the geostrophic advections of the ocean models and the horizontal and vertical Ekman advections derived from the a priori fluxes corrected with the adjusted coefficients of equation (7). The positive median value of total advection (5 W m^{-2}) is the result of the positive contribution of geostrophic advection, balanced by the weaker negative contribution of horizontal and vertical Ekman advections. Note the weak spread of both the later (IQR < 2 W m^{-2}). Finally, the individual residuals were obtained as the difference between the tendency estimated from the mean CTDs,
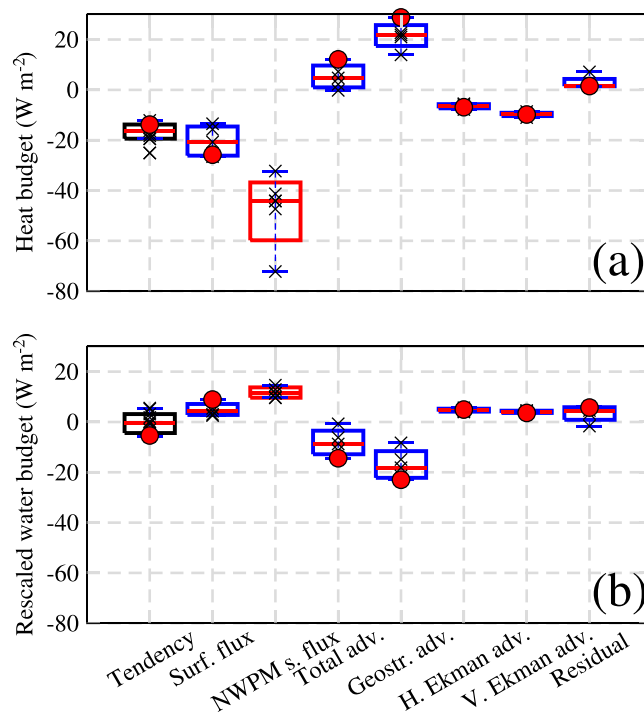
Figure 12. Box and whisker plot of the (a) heat and (b) rescaled water budgets (in W m^{-2}) in the test area for the period 1 August 2012 to 29 June 2013 (333 days). From left to right: the black box represents the lower and upper quartiles of the tendency term (seven estimates); the blue box the lower and higher quartile of the four flux retrievals obtained after replacing the MERCATOR geostrophic advection by the SYMPHONY, MARS3D, and MEDRYS geostrophic advections; the red box corresponds to the five NWPM surface fluxes (ARPEGE, AROME, NCEP, ECMWF, and ERA-INTERIM); the last five blues boxes are the lower and higher quartiles of total advection, geostrophic advection, horizontal Ekman advection, vertical Ekman advection and the residual (four estimates each). Individual estimates are represented by an X; medians are represented by red horizontal lines, and the maximum and minimum values after discarding outliers are represented by blue lines joined by blue vertical dotted lines.

minus the adjusted net heat flux and total advection from the various models. The residuals (last column in Figure 12a) are weak with a poor spread (median = 1 W m^{-2}, IQR = 3 W m^{-2}).

This means that the heat budget, estimated from various data sets and model outputs, can be considered almost closed with the adjusted fluxes. This is not the case with the NWPM fluxes, for which the heat budget is far from closure. The median of the residuals obtained with the NWPM fluxes and calculated with the tendency deduced from the CTDs (-12 W m^{-2}) and with the MERCATOR geostrophic advection (which, added with the horizontal and vertical advections, gives $+12$ W m^{-2}), is estimated to 20 W m^{-2} (the fluxes from AROME, ARPEGE, NCEP, ERA-INTERIM, and ECMWF are, respectively, -44, -72, -47, -32, and -41 W m^{-2}), i.e., nearly the same order of magnitude as the geostrophic advection term. Actually, NWPM provide surface fluxes computed without any oceanic constraint, apart from the SSTs used in bulk parameterization. On the contrary, the inverse method applied in the present study is highly constrained by the realistic simulation of the underlying whole water column and in particular by the observed heat and water budgets through the minimization of the cost function.

Note that with our best flux estimates (represented by the red dots in Figure 12a), the negative tendency term results from the balance between the dominant negative surface flux term and the positive geostrophic advection term, plus the both slightly negative horizontal and vertical Ekman advection terms. This result means that during the period considered, advection, mostly its geostrophic component, was actively bringing heat from the surroundings toward the convective area in compensation of the surface heat loss. In addition, Figure 12a shows that errors on the adjusted fluxes can be mainly attributed to errors on geostrophic advection of temperature, an important term in the first top 150 m (see Figure 5).

The same budget was estimated for salinity (Figure 12b). The different terms (multiplied by $\rho_0 C_p$ times the saline contraction coefficient and divided by the thermal expansion coefficient) were rescaled into W m^{-2} to be compared with the heat budget. The median of the tendency term is close to zero, meaning that between MOOSE 2012 and MOOSE 2013, the various estimates led to a quasi-balance between positive surface fluxes and negative advection. Positive surface fluxes correspond to an excess of evaporation over precipitation rates over the test area. Figure 12b also allows to conclude that the water budget is less well closed than for heat (the median of the residual is $+5$ W m^{-2} compared with $+1$ W m^{-2} for heat). This is mainly due to the spread of geostrophic advection (IQR = 11 W m^{-2}), larger than the spread of geostrophic advection for heat (IQR = 8 W m^{-2}). This illustrates the importance of salt injection into the area of interest. As mentioned in the previous section, all the NWPM water fluxes overestimate the adjusted E-P budget because all the residuals estimated with the NWPM are higher (median = 7 W m^{-2}) than the ones obtained with the adjusted fluxes.

6. Conclusions

Two sets of surface fluxes were produced. The first one, or a priori flux data set, on an area of 300 km × 300 km in the north-western Mediterranean (NWM), the second on a wider area (1000 km × 700 km). The first a priori data set was obtained from the best available products collected from several platforms (satellites and model outputs) to calculate each component of the surface heat and water fluxes on a 0.02° longitude × 0.02° latitude grid. These fluxes, spatially averaged, were used to force a single-column model (SCM) and to simulate the evolution of mean potential temperature and salinity profiles for this region. Through the specific form of its equations, the SCM was able to represent the evolution of subgrid scales. The SCM was forced by advection terms: horizontal and vertical Ekman advections deduced from the a priori fields, and geostrophic advection deduced from a 3-D model, which, by assimilating altimetry, represented realistically the large-scale oceanic circulation of the NWM.

After running some 50,000 SCM simulations, chosen by a genetic algorithm in varying seven control parameters—two model parameters and five coefficients correcting the surface fluxes—a best simulation was obtained. Using the optimized set of control parameters, the hourly surface a priori fluxes were corrected at each point of the grid on which they were initially calculated (resolution: hourly, on a 0.02° longitude × 0.02° latitude grid) as well as on a larger domain covering the north-western Mediterranean Sea (resolution: hourly, on a 0.04° longitude × 0.04° latitude grid): this is the second surface flux data set, or adjusted fluxes. This data set was thus directly derived from the closure of the heat and water budgets observed in the region. Indeed, with the optimization by the genetic algorithm, the model trajectory was forced to be close to the observations used in the cost function. This means that in the inverse method, the fluxes were highly constrained by the underlying ocean layers, and not only by SSTs, as was the case with the a priori fluxes. More generally, in NWPM, in satellite retrievals, and in fluxes merged from model outputs and from satellite retrievals, SSTs are the only weak oceanic constraint acting on the surface fluxes. Accordingly, the examples provided in section 5, which compare the ARPEGE, AROME, NCEP, ECMWF and ERA-INTERIM models, not only display a large spread but also a poor capacity to close the heat and water budgets of the NWM.

The ultimate goal of surface fluxes is to force three-dimensional ocean models and to simulate realistically the surface layers without any flux correction or relaxation, to obtain a correct description of surface, mid-depth and deep water masses, and to produce an oceanic circulation in agreement with the water masses produced. The same inverse method has already been applied successfully in a low-energetic region of the north-east Atlantic [*Caniaux et al.*, 2005b]. Here we showed that the same inverse method could be applied with only minor adaptation in a distinct, more energetic area, characterized by intermittent wintertime deep convection. The flux data set produced, which takes into account the oceanic mesoscale, is thought to improve simulations in this area of the Mediterranean Sea, more precisely the intensity and timing of oceanic deep convective events, and to help reduce errors on surface fluxes, the major problem of numerical simulations in this basin [e.g., *Tsimplis et al.*, 2006; *Béranger et al.*, 2010; Jordà et al., submitted manuscript, 2017]. It would be interesting to test the method in other places of the world ocean, but they need to be very well sampled to constrain the cost function. For obvious sampling reasons, we doubt that the method could be expanded to the global ocean. However, fluxes of the two test regions where the method was implemented provide a solid reference for calibrating other flux datasets, since we are not aware of any similar flux series able to close observed heat and water budgets.

References

Alhammoud, B., C. Claud, B. M. Fanatsu, K. Béranger, and J.-P. Chaboureau (2014), Patterns of precipitation and convection occurrence over the Mediterranean basin derived from a decade of microwave satellite observations, *Atmosphere*, *5*, 370–398, doi:10.3390/atmos5020370.

Anderson, R. J. (1993), A study of wind stress and heat flux over the open ocean by the inertial-dissipation method, *J. Phys. Oceanogr.*, *23*, 2153–2161.

Artale, V., D. Iudicone, R. Santoleri, V. Rupolo, S. Marullo, and F. D'Ortenzio (2002), Role of surface fluxes in ocean general circulation models using satellite sea surface temperature: Validation of and sensitivity to the forcing frequency of the Mediterranean thermohaline circulation, *J. Geophys. Res.*, *107*(C8), doi:10.1029/2000JC000452.

Barnier, B., L. Siefridt, and P. Marchesiello (1995), Thermal forcing for a global ocean circulation model using three-year climatology of ECMWF analyses, *J. Mar. Syst.*, *6*, 363–380.

Béranger, K., B. Barnier, S. Gulev, and M. Crépon (2006), Comparing 20 years of precipitation estimates from different sources over the world ocean, *Ocean Dyn.*, *56*, 104–138.

Béranger, K., Y. Drillet, M.-N. Houssais, P. Testor, R. Bourdallé-Badie, B. Alhammoud, A. Bozec, L. Mortier, P. Bouruet-Aubertot, and M. Crépon (2010), Impact of the spatial distribution of the atmospheric forcing on water mass formation in the Mediterranean Sea, *J. Geophys. Res.*, *115*, C12041, doi:10.1029/2009JC005648.

Bignami, F., S. Marullo, R. Santoleri, and M. E. Schiano (1995), Longwave radiation budget in the Mediterranean Sea, *J. Geophys. Res.*, *100*, 2501–2514.

Bourassa, M., et al. (2013), High latitude ocean and sea ice surface fluxes: Challenges for climate research, *Bull. Am. Meteorol. Soc.*, *94*(3), 403–423, doi:10.1175/BAMS-D-11-00244.1.

Bourlès, B., P. Brandt, G. Caniaux, M. Dengler, Y. Gouriou, E. Key, R. Lumpkin, F. Marin, R. L. Molinari, and C. Schmid (2007), African Monsoon Multidisciplinary Analysis (AMMA): Special measurements in the tropical Atlantic, *CLIVAR Newsl. Exchanges*, *41*(12), 7–9.

Bouttier, F. (2007), The forthcoming AROME regional forecasting system, *La Météorol.*, *58*, 12–20, doi:10.4267/2042/18203.

Bowman, K. P., C. R. Homeyer, and D. G. Stone (2009), A comparison of oceanic precipitation estimates in the tropics and subtropics, *J. Appl. Meteorol. Climatol.*, *48*, 1335–1344.

Brisson, A., P. Le Borgne, and A. Marsouin (1999), Surface solar irradiance retrieval from GOES data in the framework of the Ocean and Sea Ice Satellite Application Facility, paper presented at the 1999 EUMETSAT Meteorological Satellite Data User's Conference, EUMETSAT, Copenhagen, Danmark, 6–10 Sept.

Brisson, A., P. Le Borgne, and A. Marsouin (2001), OSI SAF radiative fluxes: Pre-operational results, paper presented at the 2001 EUMETSAT Meteorological Satellite Data User's Conference, EUMETSAT, Antalya, Turkey, 1–5 Oct.

Brut, A., A. Butet, P. Durand, G. Caniaux, and S. Planton (2005), Air-sea exchanges in the equatorial area from the EQUALANT99 dataset: Bulk parametrizations of turbulent fluxes corrected for airflow distortion, *Q. J. R. Meteorol. Soc.*, *131*, 2497–2538, doi:10.125/qj.03.185.

Caniaux, G., and S. Planton (1998), A 3D ocean mesoscale simulation using data from the SEMAPHORE experiment: Mixed layer heat budget, *J. Geophys. Res.*, *103*, 25,081–25,099.

Caniaux, G., A. Brut, D. Bourras, H. Giordani, A. Paci, L. Prieur, and G. Reverdin (2005a), A one year sea surface heat budget in the northeastern Atlantic basin during the POMME experiment: 1. Flux estimates, *J. Geophys. Res.*, *110*, C07S02, doi:10.1029/2004JC002596.

Caniaux, G., S. Belamari, H. Giordani, A. Paci, L. Prieur, and G. Reverdin (2005b), A one year sea surface heat budget in the northeastern Atlantic basin during the POMME experiment: 2. Flux optimization, *J. Geophys. Res.*, *110*, C07S03, doi:10.1029/2004JC002695.

Carroll, D. L. (1996), Genetic algorithms and optimizing chemical oxygen-iodine lasers, in *Developments in Theoretical and Applied Mechanics*, vol. XVIII, edited by H. B. Wilson et al., pp. 411–424, Sch. of Eng., Univ. of Ala., Tuscaloosa.

Castellari, S., N. Pinardi, and K. Leaman (1998), A model study of air-sea interactions in the Mediterranean Sea, *J. Mar. Syst.*, *18*, 89–114, doi: 10.1016/S0924-7963(98)90007-0.

Castellari, S., N. Pinardi, and K. Leaman (2000), Simulation of the water mass formation processes in the Mediterranean Sea: Influence of the time frequency of the atmospheric forcing, *J. Geophys. Res.*, *105*, 24,157–24,181, doi:10.1029/2000JC900055.

Colbo, K., and R. A. Weller (2009), Accuracy of the IMET sensor package in the subtropics, *J. Atmos. Oceanic Technol.*, *26*, 1867–1890, doi: 10.1175/2009JTECH0667.1.

Conan, P. (2013), DeWEX-MerMex 2013 leg2 cruise, R/V Le Suroît, SEANOE, doi: 10.17600/13020030.

Courtier, P., C. Freydier, J.-F. Geleyn, F. Rabier, and M. Rochas (1991), The ARPEGE project at Météo-France, in *ECMWF 1991 Seminar Proceedings: Numerical Methods in Atmospheric Models*, vol. 2, pp. 123–231, Eur. Cent. for Medium-Range Weather Forecasts, Reading, U. K.

Cronin, M. F., and M. J. McPhaden (1998), Upper ocean salinity balance in the western equatorial Pacific, *J. Geophys. Res.*, *103*, 27,567–27,587.

Cronin, M. F., et al. (2014), Wind stress and air-sea fluxes observations: Status, implementation and gaps, A White Paper for the Tropical Pacific Observing System of 2020 Workshop (TPOS-2020), La Jolla, Calif.

Curry, J. A., C. A. Clayson, W. B. Rossow, R. Reeder, Y. C. Zhang, P. J. Webster, G. Liu, and R. S. Sheu (1999), High-resolution satellite-derived dataset of the surface fluxes of heat, freshwater and momentum for the TOGA COARE IOP, *Bull. Am. Meteorol. Soc.*, *80*, 2059–2080.

Cushman-Roisin, B. (1987), *Dynamics of the Oceanic Surface Mixed Layer*, edited by P. Muller and D. Henderson, Hawaii Inst. of Geophys., Honolulu, Hawaii.

DeCosmo, J., K. B. Katsaros, S. D. Smith, R. J. Anderson, W. A. Osst, K. Bumke, and H. Chadwick (1996), Air-sea exchange of sensible heat and water vapor: The HEXOS results, *J. Geophys. Res.*, *101*, 12,001–12,016.

Dee, D. P., et al. (2011), The ERA-INTERIM reanalysis: Configuration and performance of the data assimilation system, *Q. J. R. Meteorol. Soc.*, *137*, 553–597, doi:10.1002/qj.828.

De Mey, P., and Y. Ménard (1989), Synoptic analysis and dynamical adjustment of GOES-3 and SEASAT altimeter eddy fields in the northwest Atlantic, *J. Geophys. Res.*, *94*, 6221–6230.

Donlon, C. J., M. Martin, J. D. Stark, J. Roberts-Jones, E. Fiedler, and W. Wimmer (2012), The Operational Sea Surface Temperature and Sea Ice analysis (OSTIA), *Remote Sens. Environ.*, *116*, 140–158, doi:10.1016/j.rse.2010.10.017.

Dourado, M. S., and G. Caniaux (2001), Surface heat budget in oceanic simulation using data from TOGA-COARE experiment, *J. Geophys. Res.*, *106*, 16,623–16,640.

Drillet, Y., J.-M. Lellouche, B. Levier, M. Drevillon, O. Le Galloudec, G. Reffray, C. Regnier, E. Greiner, and M. Clavier (2014), Forecasting the mixed-layer depth in the Northeast Atlantic: An ensemble approach, with uncertainties based on data from operational forecasting systems, *Ocean Sci.*, *10*, 1013–1029, doi:10.5194/os-10-1013-2014.

Drobinski, P., et al. (2014), HyMeX, a 10-year multidisciplinary program on the Mediterranean water cycle, *Bull. Am. Meteorol. Soc.*, *95*, 1063–1082, doi:10.1175/BAMS-D-12-00242.1.

Ducrocq, V., et al. (2014), HyMeX-SOP1, the field campaign dedicated to heavy precipitation and flash flooding in the Northwestern Mediterranean, *Bull. Am. Meteorol. Soc.*, *95*, 1083–1100, doi:10.1175/BAMS-D-12-00244.1.

Dupuis, H., C. Guérin, D. Hauser, A. Weill, P. Nacass, W. Drennan, S. Cloché, and H. Graber (2003), Impact of flow distortion corrections on turbulent fluxes estimated by the inertial dissipation method during the FETCH experiment on R/V L'Atalante, *J. Geophys. Res.*, *108*(C3), 8064, doi:10.1029/2001JC001075.

Durrieu de Madron, X., et al. (2013), Interaction of dense shelf water cascading and open-sea convection in the northwestern Mediterranean during winter 2012, *Geophys. Res. Lett.*, *40*, 1379–1385, doi:10.1002/grl.50331.

Estournel, C., et al. (2016a), HyMeX-SOP2: The field campaign dedicated to dense water formation in the northwestern Mediterranean, *Oceanography*, *29*(4), 196–206, doi:10.5670/oceanog.2016.94.

Estournel, C., et al. (2016b), High resolution modeling of dense water formation in the north-western Mediterranean during winter 2012-2013: Processes and budget, *J. Geophys. Res.*, *121*, 5367–5392, doi:10.1002/2016JC011935.

Eymard, L., et al. (1999), Surface fluxes in the North Atlantic current during CATCH/FASTEX, *Q. J. R. Meteorol. Soc.*, *125*(561), 3563–3599.

Fairall, C. W., E. F. Bradley, J. E. Hare, A. A. Grachev, and J. B. Edson (2003), Bulk parameterization of air-sea fluxes: Updates and verification for the COARE algorithm, *J. Clim.*, *16*(4), 571–591.

Feng, M., P. Hacker, and R. Lukas (1998), Upper ocean heat and salt balances in response to a westerly wind burst in the western equatorial Pacific during TOGA COARE, *J. Geophys. Res.*, *103*, 10,289–10,311.

Garreau, P., V. Garnier, and A. Schaeffer (2011), Eddy resolving modelling of the Gulf of Lions and Catalan Sea, *Ocean Dyn.*, *61*, 991–1003, doi:10.1007/s10236-011-0399-2.

Gascard, J. C. (1978), Mediterranean deep water formation, baroclinic instability and oceanic eddies, *Oceanol. Acta*, *1*, 315–330.

Gaspar, P., Y. Grégoris, and J.-M. Lefèvre (1990a), A simple eddy kinetic energy model for simulations of the oceanic vertical mixing: Test at station PAPA and long-term upper ocean study site, *J. Geophys. Res.*, *95*, 16,179–16,193.

Gaspar, P., J.-C. André, and J.-M. Lefèvre (1990b), The determination of latent and sensible heat fluxes at the ocean-atmosphere interface viewed as an inverse problem, *J. Geophys. Res.*, *95*, 16,169–16,178.

Giordani, H., G. Caniaux, L. Prieur, A. Paci, and S. Giraud (2005), A one year mesoscale simulation of the northeast Atlantic: Mixed layer heat and mass budgets during the POMME experiment, *J. Geophys. Res.*, *110*, C07S08, doi:10.1029/2004JC002765.

Giordani, H., P. Testor, L. Coppola, L. Prieur, I. Taupier-Letage, M.-N. Bouin, G. Caniaux, C. Lebeaupin, M. Hermann, and F. D'Ortenzio (2014), A multiplatform fine scale 3D analysis of the Northwestern Mediterranean during the HyMeX/ASICS Experiment: Application to dense water formation, paper presented at HyMeX 8th International Workshop, University of Malta, Valletta, 15-18 Sept.

Grist, J. P., and S. A. Josey (2003), Inverse analysis adjustment of the SOC air-sea flux climatology using ocean heat transport constraints, *J. Clim.*, *16*, 3274–3295.

Groeskamp, S., J. D. Zika, B. M. Sloyan, T. J. McDougall, and P. C. McIntosh (2014), A thermohaline inverse method for estimating diathermo-haline circulation and mixing, *J. Phys. Oceanogr.*, *44*(10), 2681–2697.

Hamon, M., et al. (2016), Design and validation of MEDRYS: A Mediterranean Sea reanalysis over the period 1992-2013, *Ocean Sci.*, *12*, 577–599, doi:10.5194/os-12-577-2016.

Herrmann, M., and S. Somot (2008), Relevance of ERA40 dynamical downscaling for modeling deep convection in the Mediterranean Sea, *Geophys. Res. Lett.*, *35*, L04607, doi:10.1029/2007GL032442.

Herrmann, M., J. Bouffard, and K. Béranger (2009), Monitoring open-ocean deep convection from space, *Geophys. Res. Lett.*, *36*, L03606, doi:10.1092/2008GL036422.

Houpert, L., et al. (2016), Observations of open-ocean deep convection in the Northwestern Mediterranean Sea: Seasonal and interannual variability of mixing and deep water masses for the 2007-2013 period, *J. Geophys. Res.*, *121*, 8139–8171, doi:10.1002/2016JC011857.

Huffman, G. J., R. F. Adler, D. T. Bolvin, G. Gu, E. J. Nelkin, K. L. Bowman, E. F. Stocker, and D. B. Wolff (2007), The TRMM multi-satellite precipitation analysis: Quasi-global, multi year, combined-sensor precipitation estimates at fine scale, *J. Hydrometeorol.*, *8*, 33–55.

Isemer, H. J., J. Willebrand, and L. Hasse (1989), Fine adjustment of large scale air-sea energy flux parameterizations by direct estimates of ocean heat transport, *J. Clim.*, *2*, 1173–1184.

Jerlov, N. G. (1976), *Marine Optics, Elsevier Oceanogr. Ser.*, vol. 14, 231 pp., Elsevier, New York.

Kantha, L. H., and C. A. Clayson (1994), An improved mixed layer model for geophysical applications, *J. Geophys. Res.*, *99*, 25,235–25,266.

Killworth, P. D., D. Smeed, and A. Nurser (2000), The effects on ocean models of relaxation toward observations at the surface, *J. Phys. Oceanogr.*, *30*, 160–174.

Large, W. G., and S. G. Yeager (2009), The global climatology of an interannually varying air–sea flux data set, *Clim. Dyn.*, *33*(2–3), 341–364.

Large, W. G., J. C. McWilliams, and S. Doney (1994), Ocean vertical mixing: A review and a model with a nonlocal boundary layer parameterization, *Rev. Geophys.*, *32*, 363–403.

Leaman, K. D., and F. Schott (1991), Hydrographic structure of the convection regime in the Golfe du Lion, *J. Phys. Oceanogr.*, *21*, 575–598.

Le Borgne, P., G. Legendre, and A. Marsouin (2007), Validation of the OSISAF radiative fluxes over the equatorial Atlantic during AMMA experiment, paper presented at the Joint 2007 EUMETSAT and American Meteorological Society Conference, EUMETSAT, Amsterdam, Netherlands, 24–28 Sept.

Liu, C., R. P. Allan, M. Berrisford, M. Mayer, P. Hyder, N. Loeb, D. Smith, P.-L. Vidale, and J. M. Edwards (2015), Combining satellite observations and reanalysis energy transports to estimate global net surface energy fluxes 1985-2012, *J. Geophys. Res. Atmos.*, *120*, 9374–9389, doi:10.1002/2015JD023264.

MacDonald, A. M., and C. Wunsch (1996), An estimate of global ocean circulation and heat fluxes, *Nature*, *382*, 436–439.

Madec, G., F. Lott, P. Delecluse, and M. Crépon (1996), Large-scale preconditioning of deep-water formation in the northwestern Mediterranean Sea, *J. Phys. Oceanogr.*, *26*, 1393–1408, doi:10.1175/1520-0485(1996)026 < 1393:LSPODW>2.0CO;2.

Marsaleix, P., F. Auclair, and C. Estournel (2009), Low-order pressure gradient schemes in sigma coordinate models: The seamount test revisited, *Ocean Modell.*, *30*, 169–177, doi:10.1016/j.ocemod.2009.06.011.

Marsaleix, P., F. Auclair, C. Estournel, C. Nguyen, and C. Ulses (2012), Alternatives to the Robert-Asselin filter, *Ocean Modell.*, *41*, 53–66, doi: 10.1016/j.ocemod.2011.11.002.

Marshall, J., and F. Schott (1999), Open-ocean convection: Observations, theory, and models, *Rev. Geophys.*, *37*(1), 1–64.

McDougall, T. J. (1987), Neutral surfaces, *J. Phys. Oceanogr.*, *17*(11), 1950–1964.

Mémery, L., G. Reverdin, J. Paillet, and A. Oschlies (2005), Introduction to the POMME special section: Thermocline ventilation and biogeochemical tracer distribution in the northeast Atlantic Ocean and impact of mesoscale dynamics, *J. Geophys. Res.*, *110*, C07S01, doi: 10.1029/2005JC002976.

Millot, C. (1987), Circulation in the Western Mediterranean Sea, *Oceanol. Acta*, *10*(2), 143–149.

Paci, A., G. Caniaux, M. Gavart, H. Giordani, M. Lévy, L. Prieur, and G. Reverdin (2005), A high-resolution simulation of the ocean during the POMME experiment: Simulation results and comparison with observations, *J. Geophys. Res.*, *110*, C07S09, doi:10.1029/2004JC002712.

Paci, A., G. Caniaux, H. Giordani, M. Lévy, L. Prieur, and G. Reverdin (2007), A high resolution simulation of the ocean during the POMME experiment: Mesoscale variability and near surface processes, *J. Geophys. Res.*, *112*, C04007, doi:10.1029/2005JC003389.

Paulson, C. A., and J. J. Simpson (1977), Irradiance measurements in the upper ocean, *J. Phys. Oceanogr.*, *7*(6), 952–956.

Persson, P. O. G., J. E. Hare, C. W. Fairall, and W. D. Otto (2005), Air-sea interaction processes in warm and cold sectors of extratropical cyclonic storms observed during FASTEX, *Q. J. R. Meteorol. Soc.*, *131*, 877–912, doi:10.1256/qj.03.181.

Pettenuzzo, D., W. G. Large, and N. Pinardi (2010), On the corrections of ERA-40 surface flux products consistent with the Mediterranean heat and water budgets and the connection between basin surface total heat flux and NAO, *J. Geophys. Res.*, *115*, C06022, doi:10.1029/2009JC005631.

Pfeifroth, U., R. Mueller, and B. Ahrens (2013), Evaluation of satellite-based and reanalysis precipitation data in the tropical Pacific, *J. Appl. Meteor. Climatol.*, *52*, 634–644, doi:10.1175/JAMC-D-12-049.1.

Pickart, R. S., M. A. Spall, M. H. Ribergaard, G. W. K. Moore, and R. F. Milliff (2003), Deep convection in the Irminger Sea forced by the Greenland tip jet, *Nature*, *424*, 152–156, doi:10.1038/nature01729.

Poulain, P. M., M. Menna, and E. Mauri (2012), Surface geostrophic circulation of the Mediterranean Sea derived from drifter and satellite altimeter data, *J. Phys. Oceanogr.*, *42*(6), 973–990, doi:10.1175/JPO-D-11-0159.1.

Redelsperger, J.-L., C. D. Thorncroft, A. Diedhiou, T. Lebel, D. J. Parker, and J. Polcher (2006), African monsoon multidisciplinary analysis: An International Research Project and Field Campaign, *Bull. Am. Meteorol. Soc.*, *87*, 1739–1746.

Rhein, M. (1995), Deep water formation in the western Mediterranean, *J. Geophys. Res.*, *100*, 6943–6959, doi:10.1029/94JC03198.

Romanou, A., G. Tselioudis, C. S. Zerefos, C. A. Clayson, J. A. Curry, and A. Andersson (2010), Evaporation-precipitation variability over the Mediterranean and the Black Seas from satellite and reanalysis estimates, *J. Clim.*, *23*, 5268–5287, doi:10.1175/2010JCLI3525.1.

Roquet, H., S. Planton, and P. Gaspar (1993), Determination of ocean surface heat fluxes by a variational method, *J. Geophys. Res.*, *98*, 10,211–10,221.

Rosati, A., and K. Miyakoda (1988), A general circulation model for upper ocean simulation, *J. Phys. Oceanogr.*, *18*, 1601–1626.

Ruti, P. M., S. Marullo, F. D'Ortenzio, and M. Tremant (2008), Comparison of analyzed and measured wind speeds in the perspective of oceanic simulations over the Mediterranean basin: Analyses, QuikSCAT and buoy data, *J. Mar. Syst.*, *70*, 33–48.

Sanchez-Gomez, E., S. Somot, S. A. Josey, C. Dubois, N. Elguindi, and M. Déqué (2011), Evaluation of Mediterranean Sea water and heat budgets simulated by an ensemble of high resolution regional climate models, *Clim. Dyn.*, *37*, 2067–2086, doi:10.1007/s00382-011-1012-6.

Send, U., J. Font, G. Krahmann, C. Millot, M. Rhein, and J. Tintore (1999), Recent advances in observing the physical oceanography of the western Mediterranean Sea, *Prog. Oceanogr.*, *44*, 37–64.

Serreze, M. C., A. Barrett, and F. Lo (2005), Northern high latitude precipitation as depicted by atmospheric reanalyses and satellite retrievals, *Mon. Weather Rev.*, *133*, 3407–3430.

Shigemitsu, M., T. Okunishi, J. Nishioka, H. Sumata, T. Hashioka, M. N. Aita, S. L. Smith, N. Yoshie, N. Okada, and Y. Yamanaka (2012), Development of a one-dimensional ecosystem model including the iron cycle applied to the Oyashio region, western subartic Pacific, *J. Geophys. Res.*, *117*, C06021, doi:10.1029/2011JC007689.

Simmons, H. L., and I. V. Polyakov (2004), Restoring and flux adjustment in simulating variability of an idealized ocean, *Geophys. Res. Lett.*, *31*, L16201, doi:10.1029/2004GL020197.

Simonot, J. Y., and H. Le Treut (1986), A climatological field of mean optical properties of the world ocean, *J. Geophys. Res.*, *91*, 6642–6646.

Smith, S. D. (1980), Wind stress and heat flux over the ocean in gale force winds, *J. Phys. Oceanogr.*, *19*, 1208–1221.

Smyth, W. D., D. Hebert, and J. N. Moum (1996), Local ocean response to a multiphase westerly burst: 1. Dynamic response, *J. Geophys. Res.*, *101*, 22,495–22,512.

Stammer, D., K. Ueyoshi, A. Köhl, W. G. Large, S. A. Josey, and C. Wunsch (2004), Estimating air-sea fluxes of heat, freshwater and momentum through global ocean data assimilation, *J. Geophys. Res.*, *109*, C05023, doi:10.1029/2003JC002082.

Sumata, H., F. Kauker, R. Gerdes, C. Köberle, and M. Karcher (2013), A comparison between gradient descent and stochastic approaches for parameter optimization of a sea ice model, *Ocean Sci.*, *9*, 609–630, doi:10.5194/os-9-609-2013.

Testor, P. (2013), DeWEX-MerMex 2013 leg1 cruise, R/V Le Suroît, SEANOE, doi:10.17600/13020010.

Testor, P., L. Coppola, and L. Mortier (2012), 2012 MOOSE-GE cruise, R/V Le Suroît, SEANOE, doi:10.17600/12020030.

Testor, P., L. Coppola, and L. Mortier (2013), 2013 MOOSE-GE cruise, R/V Le TethysII, SEANOE, doi:10.17600/13450110.

Trenberth, K. E. (1997), Using atmospheric budgets as a constraint on surface fluxes, *J. Clim.*, *10*, 2796–2809.

Tsimplis, M. N., et al. (2006), Chapter 4 Changes in the oceanography of the Mediterranean sea and their link to climate variability, in *Mediterranean Climate Variability, Dev. Earth Environ. Sci.*, vol. 4, edited by P. Lionello, P. Malanotte-Rizzoli, and R. Boscale, pp. 227–282, Elsevier, Amsterdam, doi:10.1016/S1571-9197(06)80007-8.

Valdivieso, M., et al. (2015), An assessment of air-sea heat fluxes from ocean and coupled reanalyses, [Online] *Clim. Dyn.*, doi:10.1007/s00382-015-2843-3.

Wade, M., G. Caniaux, Y. DuPenhoat, M. Dengler, H. Giordani, and R. Hummels (2011), A one-dimensional modeling study of the diurnal cycle in the equatorial Atlantic at the PIRATA buoys during the EGEE-3 campaign, *Ocean Dyn.*, *61*(1), 1–20, doi:10.1007/s10236-010-0337-8.

Waldman, R., et al. (2016), Estimating dense water volume and its evolution for the year 2012-2013 in the Northwestern Mediterranean Sea: An observing system simulation experiment approach, *J. Geophys. Res.*, *121*, 6696–6716, doi:10.1002/2016JC011694.

Yu, L., and R. A. Weller (2007), Objectively analyzed air-sea heat fluxes for the global ice-free oceans (1981-2005), *Bull. Am. Meteorol. Soc.*, *88*, 527–539, doi:10.1175/BAMS-88-4-527.

Yu, L., R. A. Weller, and B. Sun (2004), Improving latent and sensible heat flux estimates for the Atlantic Ocean (1988–1999) by a synthesis approach, *J. Clim.*, *17*, 373–393.

Yuan, D., and M. M. Rienecker (2003), Inverse estimation of sea surface flux over the equatorial Pacific Ocean: Seasonal cycle, *J. Geophys. Res.*, *108*(C8), 3247, doi:10.1029/2002JC001367.